A decadal survey of the near-surface seismic velocity response to hydrological variations in Utah, United States

Kuan-Fu Feng[1,2], Marine Denolle[1], Fan-Chi Lin[2], and Tonie van Dam[2]

[1] Department of Earth and Space Sciences, University of Washington, United States

[2] Department of Geology and Geophysics, University of Utah, United States

Corresponding author: Kuan-Fu Feng (kffeng@uw.edu)

Non-peer-reviewed preprint submitted to *EarthArXiv*. It is in the process of reviewing of the *Journal of Geophysical Research: Solid Earth*

A decadal survey of the near-surface seismic velocity response to hydrological variations in Utah, United States

Kuan-Fu Feng[1,2], Marine Denolle[1], Fan-Chi Lin[2], and Tonie van Dam[2]

[1] Department of Earth and Space Sciences, University of Washington, United States

[2] Department of Geology and Geophysics, University of Utah, United States

Corresponding author: Kuan-Fu Feng (kffeng@uw.edu)

Key Points:

- Multi-year wet-dry water cycles are closely consistent with dv/v observations, notably at stations within the Great Salt Lake watershed.
- The annual dv/v variations and their peak times are closely corresponding to expected water cycle patterns in Utah.
- Using long-term lake level as a groundwater proxy in modeling reveals regional recharge timing differences driven by elevation and snowmelt.

Abstract

Ongoing climate change leads to an increase in prolonged drought and severe weather events in the United States, particularly pronounced in semi-arid regions such as the western United States. It could have lasting social and environmental impacts. Continuous monitoring of near-surface hydrological processes and groundwater resources will provide helpful information for effective water resource management. The seismological signature of groundwater fluctuations is clear in the temporal variations in seismic velocities, dv/v. To this end, developing a proxy for groundwater level using dv/v is an opportunity but requires further understanding of the relation between dv/v and subsurface hydrology. In this study, we apply single-station cross-component correlation analysis to 28 broadband seismic stations in Utah between January 2006 and March 2023 and analyze the dv/v in the 2-4 Hz frequency band. To explain dv/v, we linearly superimpose thermoelastic stresses, soil moisture estimated from remote sensing data products, and a long-term deep water table pore pressure. We find that the relative contributions of each depend on the location, but adding a long-term water table decline, which is not systematically observed in soil moisture, better fits our data. We conclude that soil moisture alone does not explain the variations in total water storage when subsurface moisture is decoupled from the deep water table. We also conclude that dv/v can be used as a proxy for water storage.

Plain Language Summary

Climate change is causing more frequent and intense droughts and severe weather in the western United States, especially in semi-arid areas. This situation could have severe social and environmental consequences. To manage water resources effectively, continuously monitoring groundwater and related hydrological processes is important. Changes in groundwater levels can be detected through variations in seismic velocities, known as dv/v. This study aims to understand how these seismic changes relate to near-surface water by analyzing data from 28 broadband seismic stations in Utah from January 2006 to March 2023. We focus on seismic signals in the 2-4 Hz frequency range and combine these signals with information about thermal stresses, soil moisture from remote sensing, and long-term deep groundwater table. Our findings indicate that the importance of each factor varies by location. However, incorporating long-term groundwater decline better matches our observations. We conclude that soil moisture alone cannot fully explain changes in total water storage when disconnected from deeper groundwater levels. Ultimately, we suggest that dv/v can serve as a useful indicator of water storage in the subsurface.

1 Introduction

Widespread droughts and extreme weather events have become more common in recent years as a result of ongoing climate change (Coumou and Rahmstorf, 2012; Hulme, 2014). The increasing frequency and severity of droughts could lead to enduring impacts on society and the environment (Schwabe et al., 2013; Khatri and Strong, 2020). Utah is situated in a semi-arid region of the western US, characterized by limited water availability. Water resource management is always a crucial issue for the state. The water supply in Utah is precipitation in the form of snowpack. The snowpack accumulates in the winter, and groundwater and stream flow control the runoff during the dry season. There are several lakes and reservoirs across the state that capture snowmelt runoff. The Great Salt Lake (GSL) is the largest terminal lake in Northern America and serves as the terminus for various rivers, streams, and subsurface groundwater within its extensive catchment area. Due to its salinity, GSL does not directly contribute to the regional water supply, but its water level has been considered one of the primary indicators of regional water resources. The GSL has experienced periods of extended drought throughout its history, including years of shortages and years of replenishment (Wang et al., 2012; Utah Division of Water Resources, https://water.utah.gov/great-salt-lake/, last accessed 01/2023). Nowadays, it is facing the challenges of declining water levels, which have reduced by more than 3 meters since 1999 (Hassan et al., 2023). Prolonged droughts can severely impact the lake's ecosystem and overall health (Baxter and Butler, 2020; Null and Wurtsbaugh, 2020). The uncertainty associated with the groundwater inflow, however, makes it difficult to assess the GSL water budget accurately.

Conventionally, monitoring groundwater levels, whether they reside in aquifers or as subsurface moisture, requires in-situ instrumentation (i.e., wells and probes) with local sensitivities. These measurements are a site's ground truth for water storage but have two limitations. First, data collection of ground-based sensors has historically been varied. Second, advancements are being made in data collection and distribution (e.g., Perrone and Jasechk, 2017). Alternatively, remote sensing provides increasingly frequent measurements (~3 days) and a large spatial footprint (~10-35 km) (e.g., Tangdamrongsub et al., 2020). Temporal water mass variation on a much larger scale can be monitored through remote sensing (e.g., GRACE; Landerer and Swenson, 2012) despite the relatively low spatial resolution at around a few kilometers to hundreds of kilometers. For subsurface moisture, Ford and Quiring (2019) performed a comprehensive comparison between soil moisture measurements, especially comparing in-situ with modeled products and remote-sensing-based derived estimates. They concluded that both the Northern American Land Data Assimilation System project phase 2 (NLDAS-2) and the Soil Moisture Active Passive (SMAP) consistently performed best. Improved parameterization, models, or proxies of near-surface water remain a desirable avenue of research.

Recently, the seismology community has demonstrated the possibility of linking seismic velocity changes (dv/v) with hydrological variations, where intermediate spatial sensitivity and resolution from a few meters to kilometers can be achieved. The time resolution ranges from hours to decades, depending on the station operation period and research purpose. Many studies have reported a strong (anti-)correlation (e.g., instantaneous response) between perturbation in seismic velocities and subsurface hydrological variables such as groundwater level changes and soil moisture variations (Sens-Schönfelder and Wegler, 2006; Gassenmeier et al., 2014; Voisin et al., 2016; Lecocq et al., 2017; Clements and Denolle, 2018; Illien et al., 2021; Oakley et al., 2021; Mao et al., 2022; Shen et al., 2024). Because the method only relies on passive seismic noise and seismic stations can be deployed relatively easily, this technique might provide a cost-efficient way to monitor subsurface hydrological parameters at the mesoscale. This method, so-called time-lapse passive seismic interferometry, measures coda waves perturbations from repeating waveforms and infers dv/v. The repeated waveform can be obtained from either repeated sources or noise correlation functions calculated using different time windows (Snieder et al., 2002; Weaver and Lobkis, 2004; Pacheco and Snieder, 2005; Sens-Schönfelder and Wegler, 2006).

Variations in groundwater levels in the subsurface induce local changes in effective pressure, leading to changes in seismic velocities. In fully saturated media, e.g., below the water table, changes in rigidity, the ability of rocks to resist shear stresses, are reduced with increasing pore pressure. This leads to a reduction in shear wave speed. Density changes due to pore pressure changes are not large because of the incompressibility of rocks and water (Fokker et al., 2021). dv/v has been correlated with dilatational strains empirically (Donaldson et al., 2019; Sens-Schönfelder and Eulenfeld, 2019; Takano et al., 2019; Hotovec-Ellis et al., 2022) and as predicted from the earthquake-related drop/healing behaviors or temperature-humidity coupling effects under a non-linear elasticity framework (Ostrovsky and Johnson, 2001; Hobiger et al., 2014; Clements and Denolle, 2023; Diewald et al., 2024; Okubo et al., 2024). Above the water table, in partially saturated media, both rigidity and density are affected by relative water content, and more complex physics, which depends on pore water distributions, may affect the wave speed (e.g., Solazzi et al., 2021). Seismic waves have spatial resolution and sensitivity that depend on their wavelengths: high-frequency signals can have relatively high spatial resolution (e.g., 500 m/s shallow seismic waves at 5 Hz have a 100-meter wavelength) and shallow depth sensitivity compared to low-frequency signals, considering the surface waves dominant codas (Obermann et al., 2013, 2016). Therefore, shear waves are useful to track groundwater changes at intermediate spatial resolutions. Because seismic signals are continuously recorded, they can provide continuous measurements, at least at the hourly time scale, of water levels at the mesoscale.

One outstanding issue remains on whether dv/v is measuring subsurface moisture in partially saturated media or water table changes. Indeed, the depth resolution is relatively smooth in surface waves, and conventional networks of seismometers do not permit precise depth analysis. Illien et al. (2021) were the first to propose a model that combines groundwater storage and subsurface moisture to explain the surface observations of dv/v. They relied on in-situ moisture and geochemical tracer measurements for groundwater depth to discriminate between the two water storages. They found that in Nepal, the intermittent coupling of subsurface water with groundwater during groundwater replenishment can explain the dv/v observations. While multi-sensor networks are increasingly valued and deployed (Oakley et al., 2021), they often span only short-term experiments. Here, we tackle the problem of differentiating the relative contribution between moisture and water table on a regional scale and over decades of data.

This study analyzes continuous seismic recordings of 28 broadband seismic stations across Utah (Figure 1) between January 2006 and March 2023. We use single-station measurements to determine the temporal evolution of dv/v (e.g., Hobiger et al., 2014; Feng et al., 2021; Clements and Denolle, 2023; etc.). We compare the evolutions of the observed dv/v with the GSL and Utah Lake water levels and near-surface moisture at stations to investigate the relationship between dv/v variations and the potential hydrological signatures. The observed dv/v evolutions reveal seasonality across most stations. Their annual cycles, with a positive dv/v peak time around autumn and a negative dv/v peak time around late spring to early summer, are consistent with the expected water cycle in Utah, except for a station adjacent to the human-controlled Jordanelle Reservoir. We use the evolution of the Utah Lake as an approximate functional form to model water table levels, accompanying the near-surface moisture and temperature estimates to explore dv/v.

2 Data and Methods

2.1 Time-lapse passive seismic interferometry

Time-lapse passive seismic interferometry is a method for extracting changes in seismic velocities from phase differences in the seismic coda waves that have the same source and receivers but are recorded at different times. The fundamental assumption behind passive seismic interferometry is that, for a diffusive noise field, the cross-correlation function can be approximated as the empirical Green's function (Lobkis and Weaver, 2001; Snieder et al., 2002; Weaver and Lobkis, 2004). In such a scheme, the coda of the correlation waveform is the result of multiple scattering when the direct waves pass through Earth heterogeneities (Pacheco and Snieder, 2005; Planès et al., 2014). Owing to the multiple scattering nature, coda waves take much longer paths than direct waves before arriving at the receiver station. Therefore, they are more sensitive to perturbation in the medium and less sensitive to changes in the noise source (Colombi et al., 2014). Assuming homogeneous velocity changes in the medium, the seismic velocity perturbation of the medium, in here dv/v, can be characterized by the presence of coda wave time shifts at different time lapses (Snieder et al., 2002).

2.2 Seismic data

Taking advantage of the continuous seismic recordings, this study analyzes three-component continuous broadband seismic recordings between January 2006 and March 2023 from the stations in the University of Utah Regional Seismic Network (UU) and the United States National Seismic Network (US) in Utah. To study both long-term and annual dv/v evolutions, we only include the 28 broadband stations with over five years of operation time in our analysis (Figure 1, inverted triangles). The data completeness of the 28 stations is shown in Figure S1. We perform a general standard pre-processing, which removes instrumental response, demeans, detrends, and tapers before decimating the data to 20 Hz and storing them in 1-day-long segments. We remove all component observations with data gaps in any single component and check daily waveforms in spectrograms to exclude malfunction periods.

2.3 Single station seismic dv/v measurements

We perform a single-station cross-component correlations (SC) analysis, which has been well demonstrated in investigating tectonically and environmentally driven dv/v evolutions in previous studies (e.g., Hobiger et al., 2014; De Plaen et al., 2016; Viens et al., 2018; Yates et al., 2019; Feng et al., 2021; Clements and Denolle, 2023). We adopt Welch's method (Seats et al., 2012) to improve the quality of the correlation functions. We first cut the daily three-component seismic data into 10-minute windows, detrend, taper, and apply spectral whitening in the frequency band 0.1-8 Hz. We then calculate the SC functions between each non-identical component (i.e., ZN, ZE, NE, EN, EZ, and NZ) with non-overlapping 10-minute time windows. We calculate the root mean square (RMS) amplitude for each 10-minute SC and remove all 10-minute SCs with RMS above five times the daily averaged RMS. Those windows often contain unfavorable energetic signals (e.g., earthquakes, instrumental irregularities, and non-stationary transient signals). For each station and each cross-component, we stack all remaining SCs to obtain the reference SC function and the 60-day stacked SC functions. The 60-day window is selected to gain better signal-to-noise ratios (SNR) and improve the coherence between each current SC function (Figure S2). We focus on the 2-4 Hz frequency band, where coherent SC coda signals can be observed.

Assuming the velocity change in the medium is laterally homogeneous, for each 60-day stacked SC function (as current SC function hereafter), we measure the relative velocity change dv/v compared to the reference SC function. Here, we assume that the dt/t (time shift over lag time) of the coda signal is related to dv/v via the equation (Snieder et al., 2002):

$$dt/t = -dv/v. \tag{1}$$

Equation (1) demonstrates that delayed phase shifts (dt >0) are associated with velocity reductions (dv <0). For a uniform change dv/v, the delay time increases with the lag time as propagation paths are longer for scattered waves that arrive later. We measure dv/v by band-passing the SC functions in 2-4 Hz and a selected 2-8 sec lag time coda window (Figure S2, black boxes) to reduce the effect of the energetic near-zero lag time ballistic waves. Assuming Rayleigh waves dominate the coda signal, the dv/v measurement in this frequency band is mostly sensitive to velocity changes down to 500-meter depth (Figure S3). The lateral sensitivity is ~1 km based on the first Fresnel zone approximation (Bennington et al., 2018).

We adopt the stretching method (Sens-Schönfelder and Wegler, 2006) to measure the dv/v evolutions. The reference SC (SC^{ref}) is either stretched or compressed to obtain a best-fit correlation coefficient cc(ϵ) with the current SC (SC^{cur}):

$$cc(\epsilon) = \frac{\int_{t1}^{t2} SC^{cur}(t)\, SC^{ref}\big(t(1+\epsilon)\big)dt}{\sqrt{\int_{t1}^{t2}[SC^{cur}(t)]^2 dt\ \int_{t1}^{t2}\big[SC^{ref}\big(t(1+\epsilon)\big)\big]^2 dt}} \tag{2}$$

, where ϵ is the stretching factor and t_1 and t_2 are the beginning and the ending lag time of the coda window, respectively. We perform a grid search of ϵ in a range of -2% to 2% with a 0.01% increment, and the dv/v is determined by the ϵ with the maximum cc. A weighted contribution across the six SC components is used to compute the final dv/v time series $\frac{dv}{v}_{final}$ (Hobiger et al., 2014; Viens et al., 2018):

$$\frac{dv}{v}_{final} = \frac{1}{\sum_{i=1}^{6} cc_i^2} \sum_{i=1}^{6} cc_i^2 \left(\frac{dv}{v}\right)_i \tag{3}$$

, where the cc_i and $(\frac{dv}{v})_i$ are the maximum correlation coefficient and estimated dv/v of each component after stretching. Based on a theoretical formulation of the apparent stretching factor ϵ (Weaver et al., 2011), we also calculate the uncertainty of the estimated dv/v for each cross-component via:

$$rms(\epsilon) = \frac{\sqrt{1-cc^2}}{2cc}\sqrt{\frac{6\sqrt{\frac{\pi}{2}}T}{\omega_c^2(t_2^3-t_1^3)}} \tag{4}$$

, where cc is the maximum correlation coefficient, T is the reversed of the measured frequency bandwidth, ω_c is the corner angular frequency, t_1 and t_2 are the begin and end time of the selected coda window. We present the averaged uncertainty of all components as the uncertainty of our dv/v time series (e.g., Figure 2).

2.4 Depth sensitivity and Vs30 model

Assuming strong Rayleigh waves in the coda of the single-station correlations, we use surface-waves sensitivity with depth given a shear-wave wave speed profile, taking the mean values of the grids in proximity to seismic stations from Schmandt et al. (2015), to obtain the depth sensitivity kernels as shown in Figure S3. With this framework, we find that the depth sensitivity of our measurements is in the top 150 meters. The state average water table depth is 8 m (Fan et al., 2007), though the UUSS broadband stations are mostly located away from the basins and where the water table is deeper (~10-30 m). Additional data from the United States Geological Survey (USGS) Vs30 model shows that high near-surface velocities are also expected (Heath et al., 2020).

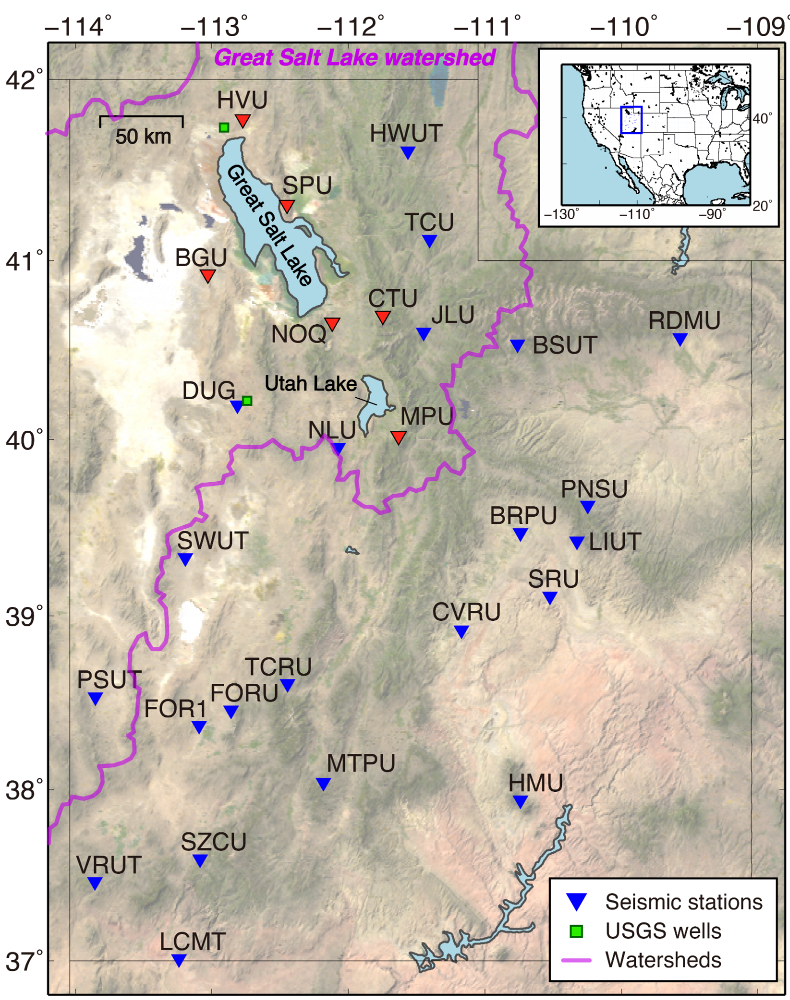

Figure 1. Station map. The inverted triangles are the broadband seismic stations used in this study. The red inverted triangles identify the stations in Figure 4. The green squares are the two closest groundwater wells used for comparison. The pink curve encircles the Great Salt Lake watershed (from the Utah Division of Water Resources, https://water.utah.gov/).

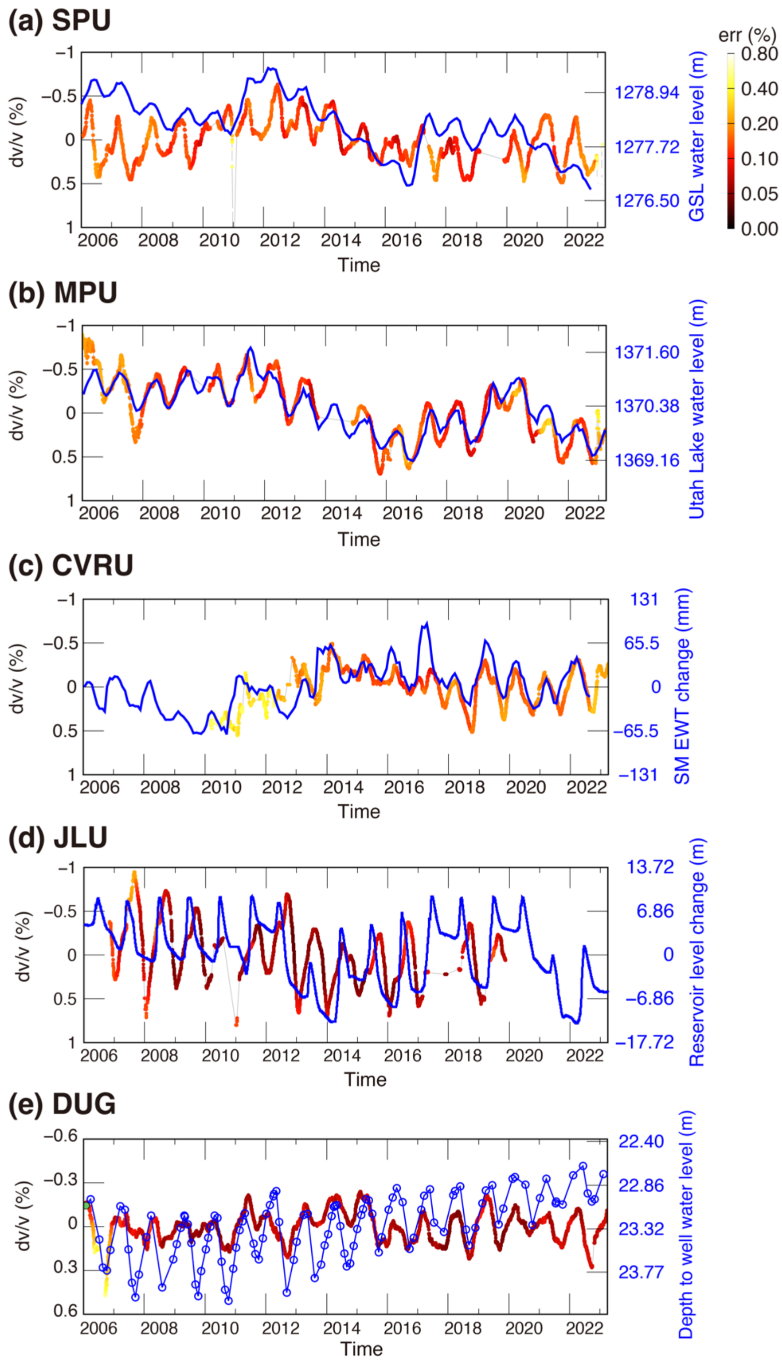

Figure 2. Co-evolutions of observed dv/v (warm-color-coded curves) and the corresponding hydrological factors (blue curves). Note the positive/negative dv/v is plotted upside down for better comparison. (a) Station SPU dv/v versus the GSL water level. (b) Station MPU dv/v versus the Utah Lake water level. (c) Station CVRU dv/v versus the corresponding soil moisture equivalent water thickness (SM-EWT). (d) Station JLU dv/v and the Jordanelle Reservoir

water level. (e) Station DUG dv/v and the nearby groundwater level record. In (a-d), the hydrological data is evenly sampled.

2.5 Hydrological and temperature data

The GSL, the largest terminal lake in Northern America, is the remnant of the larger Pleistocene Lake Bonneville. It is an essential natural and economic resource for the region. On the other hand, Utah Lake, located south of the GSL, is a freshwater lake fed by several rivers, with the Jordan River as its outlet, flowing northward into the GSL. We gather GSL water level data from USGS Water Resources (https://dashboard.waterdata.usgs.gov, last accessed 10/2022, Site No. 10010100). It shows roughly an annual water level variation of ~1.2 m (~4 ft) on top of a long-term dry-wet cycle of nearly 3 m (Figure 2a). The Utah Lake water level is estimated from the storage volume obtained from the Snowpack Telemetry (SNOTEL) Utah reservoir site (Site No. 10166500), operated by the Natural Resources Conservation Service (NRCS) of the United States Department of Agriculture (USDA, https://www.nrcs.usda.gov/, last accessed 04/2023). We estimate the water level by dividing the storage volume by the lake area of 384.4513 km^2 (95,000 Acres). Its water level has a long-term dry-wet variation (Figure 2b) similar to that of the GSL. Its annual variation is ~1 m.

Moisture in vadose zones also plays a crucial role in the near-surface water resources (Illien et al., 2021; Shen et al., 2024). However, due to the lack of co-site hydrological measurement, we characterized soil moisture equivalent water thickness (SM-EWT) derived from the NLDAS-2 (Xia et al., 2012ab) as the near-surface water content for comparison. The NLDAS was developed by a nationwide multi-institution partnership (Mitchell et al., 2004). The NLDAS system ingests various observational data, such as satellite remote sensing measurements, ground-based weather station data, and radar-based rainfall estimates. These data are assimilated into sophisticated land surface models (LSMs) to produce gridded outputs ($0.125° \times 0.125° \cong 14$ km x 14 km), including terms related to surface energy and water budgets. We extract the SM-EWT data from the closest grid point to the seismic stations (Figure S4). The locations are normally within ~9.3 km. The average annual variations of SM-EWT range from 0.05 to 0.22 m. Figure 2c shows an SM-EWT time series as an example at Station CVRU.

The Jordanelle Reservoir is a man-made reservoir about 3 km from Station JLU. It serves multiple purposes, including water storage, flood control, and recreation. Therefore, its highest and lowest water levels are different from other surface water bodies (the blue curve in Figure 2d). We collected the reservoir's monthly water levels from the United States Bureau of Reclamation (https://data.usbr.gov, last accessed 04/2023). Station JLU is located on a mountain crest. While hydraulic connectivity at the site does not appear to be linked to the reservoir, considering its proximity, its subsurface velocity variations could be affected by the reservoir's poroelastic loading in response to the 30-meter annual water level variations.

For in situ groundwater data, in our study area, most wells are in the valley and exhibit irregular time resolution for data collection. However, there are two wells managed by the USGS Utah Water Science Center (https://www.usgs.gov/centers/utah-water-science-center, last accessed 04/2023, Site No. 414411112543701 and 401312112442301), shown as green squares in Figure 1, have relatively comparable time samplings. These two wells are in proximity to seismic stations HVU and DUG (Figure 1).

In addition to hydrological terms, thermoelastic effects have also been contributing to the dv/v seasonality (Tsai, 2011; Richter et al., 2014; Fokker et al., 2024; Shen et al., 2024). Across Utah, the average air temperature change over a year ranges from below zeros to over 40 degrees Celsius. To take temperature effects into account, we collect air temperature records from the Parameter-elevation Relationships on the Independent Slopes Model (PRISM) Gridded Climate Data (PRISM Climate Group, https://prism.oregonstate.edu/, last accessed 04/2023, Daly et al., 2008). They gather climate data from numerous monitoring networks, apply advanced quality control methods, create spatial climate datasets to reveal both short-term and long-term climate patterns, and provide the PRISM, a 4 × 4 km gridded product. We collect the data from the points closest to our seismic stations. The temperature records at each station are generally similar, with the lowest temperatures typically occurring in early February and the highest around July on average with 20.4 to 28.4 degrees Celsius annual variations. We interpolated all hydrological and temperature data at daily intervals to compare them with the dv/v time series.

3 Results and analysis

3.1 Seasonality of the observed dv/v

The observed dv/v evolutions reveal strong seasonality at most stations. We perform annual stacks at all stations to investigate the seasonality of dv/v (Figures 3, S6, and S7). Figure 3c shows the annual dv/v stacks for several representative stations. Based on the annual dv/v variations, we calculate the average peak time of the highest and lowest dv/v for all stations and summarize them in Figures 3a and 3b. Considering the uncertainties of those low annual variation stations, we only plotted the stations with average annual variations above 0.3%. The amplitude of annual variations over stations is mapped in Figure S6. Overall, the average positive dv/v peak times are observed around autumn between August and October (Figure 3a), and the negative dv/v peak time appears around late spring and early summer between April and June (Figure 3b). These peak time patterns are consistent with Utah's general water cycle, which goes from October 1st to September 30th, where groundwater is lowest during the dry summer-fall months and replenishes during the spring runoff. Station JLU is unique due to its proximity to the managed reservoir. It is reasonable that it shows a different peak time than others. Looking more closely, stations HWUT and FORU have a dv/v plateau during the autumn and winter months (Figure S7) despite the peak times being slightly delayed compared to other stations (Figure 3). Stations at higher elevations tend to have a later negative peak time, likely due to the late snowmelt in the mountainous areas, although this is not so obvious.

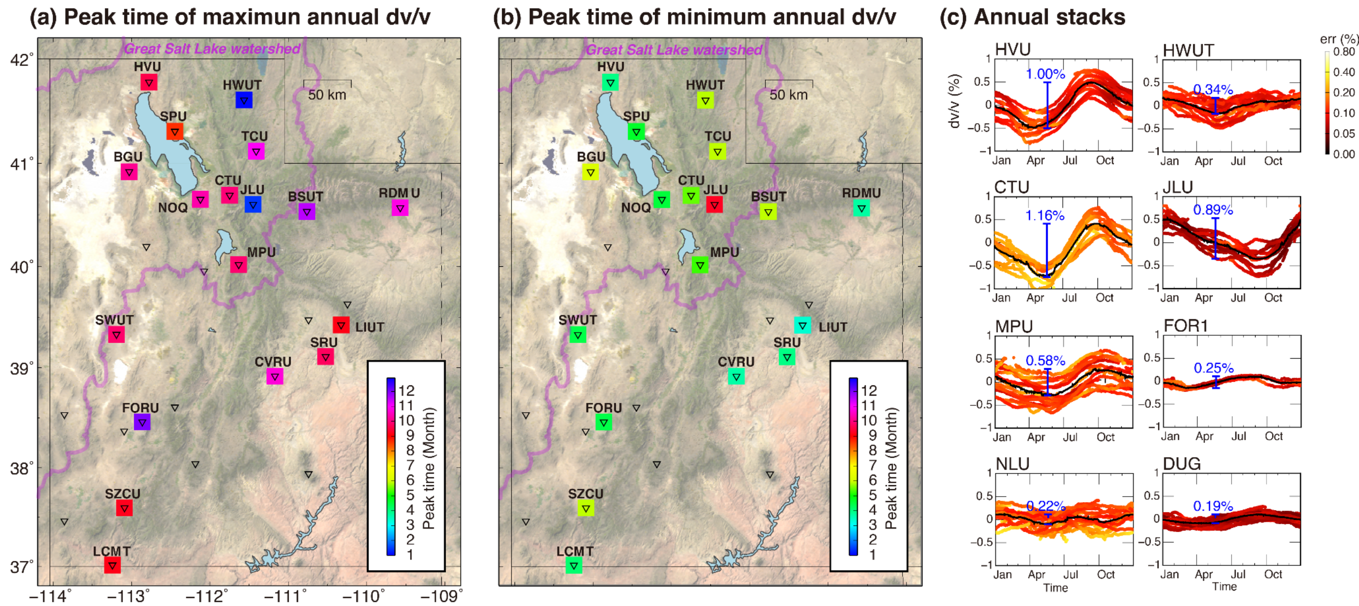

Figure 3. Peak time maps of the (a) highest and (b) lowest points in annual dv/v. The pink curve encircles the Great Salt Lake watershed. (c) Example stations of the annual dv/v stacks. The colored curves are the observed dv/v for each year, with the color representing estimated uncertainty. The black curves represent the mean. The peak-to-peak variation amplitudes of the mean are shown by the blue bars and the values on top.

3.2 Co-evolution between observed dv/v and lake water levels

The multiyear dry-wet variations of the northern Utah hydrological system are manifested by the GSL and Utah Lake water level records. The lake's water level reflects the 2007 drought and multiyear droughts in 2012-2017 and 2020-2022 (Figure 4a). Similar long-term variations are also observed by the dv/v at nearby stations in the GSL watershed (Figure 4b, those red inverted triangle stations in Figure 1). The dv/v times series are flipped to improve the visualization of the anti-co-evolution to the water levels. We see a slight down-going (increase in dv/v) in 2007 at Stations MPU and SPU. An apparent long-term decline (increase in dv/v) over the six stations appeared in 2012-2017 and the period after 2020.

The dv/v at stations within the GSL watershed generally correlate better with the lake levels than stations outside the watershed. Figures 5a and 5b and Table S1 summarize the results of correlation coefficients and R-squared values for all stations. Focusing on these stations within the watershed, Station MPU has the most significant negative correlation to the GSL and Utah Lake water levels, with values of -0.82 and -0.91, respectively. The significant correlation at Station MPU suggests that the dv/v measurement there and the Utah Lake level are sensitive to the exact same hydrological controls. The two stations near the Salt Lake Valley between the Utah Lake and GSL (Stations CTU and NOQ) show stronger correlations with the Utah Lake levels with values of -0.69 and -0.58 and a bit lower correlation to the GSL of -0.59 and -0.4. The two stations near the GSL (Stations SPU and HVU) show slightly lower correlations to the lakes, with values between -0.42 and -0.65. Surprisingly, station BGU has a stronger correlation to the Utah lake water level (-0.82) than the GSL water level (-0.67).

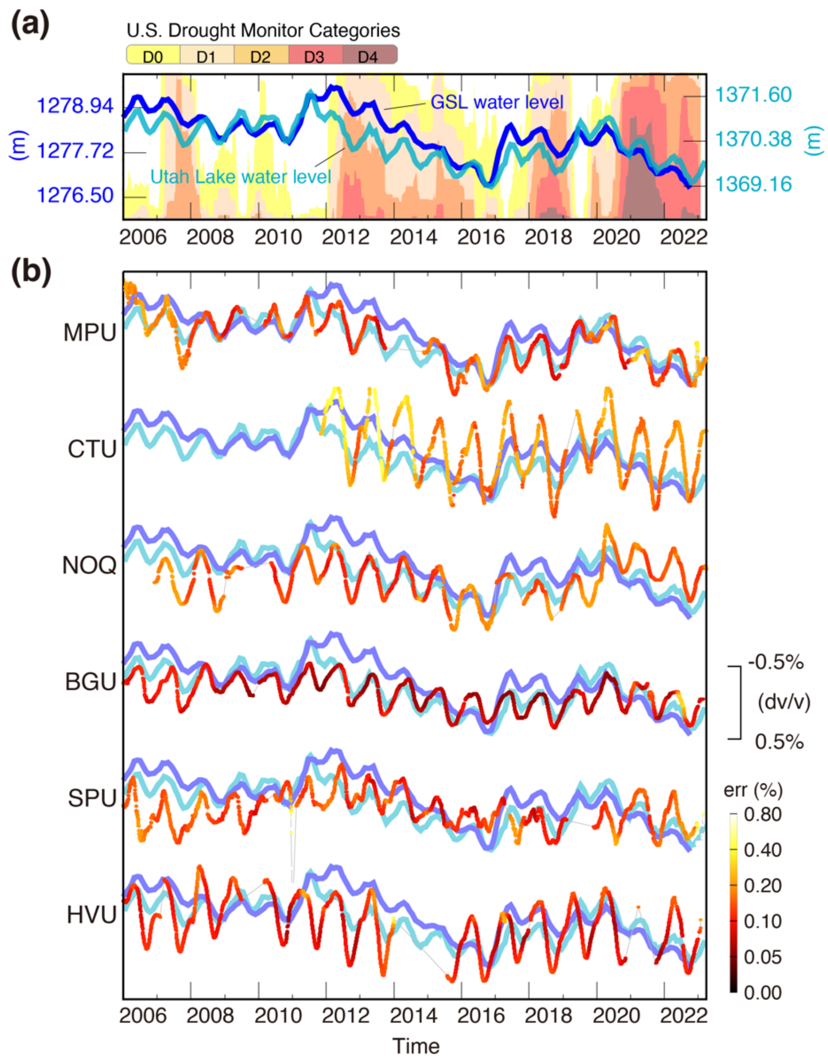

Figure 4. Co-evolution of dv/v and GSL and Utah Lake water levels. (a) Lakes' water level variations with the drought monitoring graph from the US National Integrated Drought Information System. D0 to D4 represent different drought levels, from abnormally dry (D0) conditions to exceptional drought (D4). The blue and cyan curves represent the GSL and Utah Lake records, respectively. (b) Co-evolution of flipped dv/v for stations adjacent to the lakes (red reversed triangles in Figure 1) and the water level records in (a). The color of the dv/v represents estimated uncertainty.

3.3 Correlation between dv/v and SM-EWT

The correlation coefficients between dv/v and the SM-EWT are less coherent spatially (Figure 5c), in contrast to the correlation between the lake water levels and dv/v primarily concentrated within the GSL watershed. The strongest (anti-)correlation appears at Station CTU with a value of -0.78 (highlighted by a yellow label in Figure 5c). The Stations FORU and FOR1 in southern Utah also show relatively high correlations at -0.72 and -0.6. Station CVRU (highlighted by a red label in Figure 5c) is one of the few stations deployed on a soil site, as documented by the UUSS (Farrell, pers. comm.). Although the correlation at CVRU is not the strongest, its correlation coefficient achieves -0.56. Except for Station JLU, the correlation coefficients between dv/v and SM-EWT are generally negative, agreeing with previous observations (e.g., Illien et al., 2021; Sheng et al., 2024). However, it is worth noting that we are not using the direct soil moisture measurement; instead, we are comparing our results with the equivalent water thickness from NLDAS-2 that is best correlated with *in-situ* moisture (Illien et al., 2021; Sheng et al., 2024) relative to other remotely sensed measurements during this period.

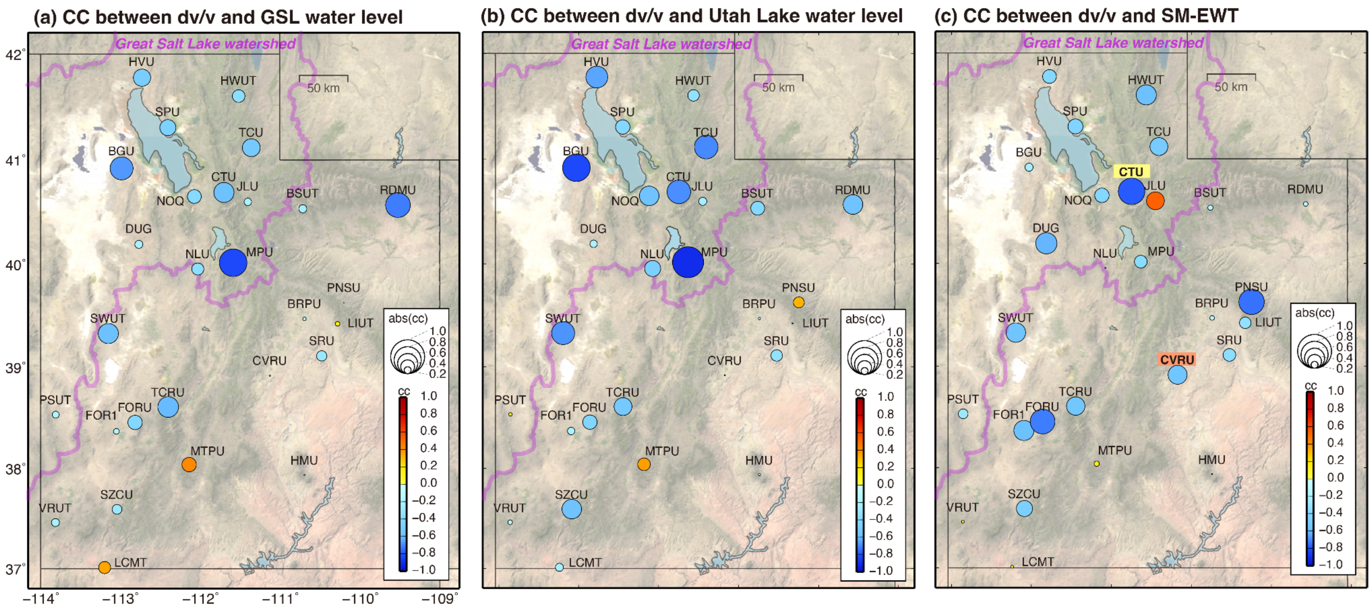

Figure 5. Correlation coefficient maps of the observed dv/v with the lakes' water level variations and SM-EWT. (a) dv/v correlation map to the GSL water level. (b) dv/v correlation map to the Utah Lake water level. (c) dv/v correlation map to the SM-EWT. The colors represent the correlation coefficient between the dv/v and the corresponding lake water level. The circle size shows the absolute value of the correlation coefficient at stations. The pink curves encircle the Great Salt Lake watershed area.

3.4 Modeling on dv/v and MCMC analysis

To understand how much each factor contributes to the system, we model dv/v with a linear combination of the factors. We identify two potential water storage that impacts seismic velocities: subsurface moisture (e.g., Oakley et al., 2021; Illien et al., 2021; Shen et al., 2024) and water-table levels (e.g., Voisin et al., 2016; Gaubert-Bastide et al., 2022). According to the depth sensitivity of our seismic signals (see Figure S3) and the average water table levels, our dv/v should sample both moisture variations and the water table at depth, and the relation between moisture and water table is decoupled. Other than that, we also consider thermoelastic stress and model it with the time-shifted surface air temperature to model the diffusion at a depth of annual temperature variations (e.g., Berger, 1975; Richter et al., 2014).

This study explores novel ways to introduce groundwater and soil moisture with temperature effects to explain seismic velocity variations dv/v. First, we use a base model formulated as

$$y_{base}(t) = A + B \cdot SMEWT(t) + C \cdot T(t - \Delta t_{tshift}) \quad (5)$$

where the parameters to fit are the constant level (A) and coefficients (B, C) to the soil moisture term, $SMEWT(t)$ and temperature term with a time shift $T(t - \Delta t_{tshift})$. Considering the long-term decline of the groundwater table over the past decades (Wada et al., 2010; Perrone and

Jasechk, 2017), we propose two models: (1) the base model in Equation 5 accompanied by a linear trend and (2) the base model in Equation 5 accompanied by a lowpass filtering lake level to synthesize water-table effects on dv/v. In the first model, a positive linear trend represents the corresponding increase in dv/v due to the long-term decline in the overall groundwater table. The first model is written as

$$y_{linear}(t) = y_{base}(t) + lineartrend(t). \tag{6}$$

In the second model, assuming the regional groundwater table pattern is similar to the lake level in the long term, we lowpass filter the Utah Lake level with a 2-year corner period to approximate the groundwater term denoted as $Lake_{lowpass}$ at any given time t, with a time shift Δt_{wshift}. The model leverages the known correlation between groundwater levels and lake levels (Ghambari and Bravo, 2011; Wu et al., 2022), also justified by the strong correlations between the GSL and the Utah Lake levels and dv/v (see Results section). This model is written as

$$y_{lowpass}(t) = y_{base}(t) + D \cdot Lake_{lowpass}(t - \Delta t_{wshift}) \tag{7}$$

where D is the coefficient of the groundwater term.

Following the steps outlined by Ermert et al. (2023) and Okubo et al. (2024), we utilize emcee, a software tool based on Python (Foreman-Mackey et al., 2013), to fit the time series in a Bayesian framework. The emcee employs the Markov chain Monte Carlo (MCMC) method and offers various advanced sampling algorithms. We adopt the stretch move method introduced by Goodman and Weare (2010) to update model parameters. This method involves a set of walkers. We configure the number of walkers as 32 and perform 12,000 iterations, with 10% discarding as burn-in. The log-likelihood function with a set of model parameters θ is referred to Okubo et al. (2024):

$$ln\,(l(\theta)) = -\frac{1}{2}\sum_n \left[\frac{(\,dvv(t_n) - y_{model}(t_n,\theta)\,)^2}{\hat{\sigma}_n^2} + ln\,(\hat{\sigma}_n^2)\right], \tag{8}$$

where σ_n is the estimated error of the dv/v, dvv is the dv/v, and y_{model} is the predicted dv/v from models y_{linear} and $y_{lowpass}$ at the time t_n, respectively. During the modeling process, we set up the parameter sampling ranges of each term based on the knowledge from previous literature, such as B is sampling in negative values due to the anti-correlation between dv/v and soil moisture (e.g., Illien et al., 2021); C should be positive due to the positive correlation between dv/v and air temperature (e.g., Richter et al., 2014), and D is negative due to the anti-correlation between dv/v and groundwater level changes (e.g., Sens-Schönfelder and Wegler, 2006). Table 1 summarizes the parameters and the corresponding sampling ranges of the model. The 90-day bounds of the time shift of temperature effect representing the thermal diffusion effects are considered an average 70-day shift from a state-wide experiment in Clements and Denolle (2023). The time shift of the assumed groundwater table is given in a range of [-182, 182] days, considering the unknown inflow and seepage (e.g., Somers and McKenzie, 2020) but only within a year-round cycle.

For modeling data preparation, we apply a 30-day rolling average to the dv/v time series to obtain smooth data comparable to other components, i.e., SMEWT, temperature, and lake level, those in monthly sampling. To align each component at the same stations, we trim them with the same starting and ending dates. All the time series have the mean values removed and have been normalized to [-1, 1]. Stations HVU and VRUT have over a year of data gaps, which will introduce biases into modeling processes. Therefore, we divided these datasets into two periods for these stations and named them HVU1, HUV2, VRUT1, and VRUT2.

Recent studies have proposed that coupling between soil moisture and groundwater, temperature, and humidity may be necessary (e.g., Sens-Schönfelder and Eulenfeld, 2019; Illien et al., 2021; Diewald et al., 2024). However, apart from dv/v observation, we don't have in-situ measurements as they did; therefore, we would need to ignore this complexity in this study.

Table 1. Model parameters and the ranges used for the MCMC sampling.

Variable	Description	Sampling range [min, max]
A	offset of dv/v	[-1.0 , 1.0] %
B	factor of soil moisture equivalent water thickness	[$-\infty$, 0]
C	factor of temperature	[0 , ∞]
Δt_tshift	time shift of the temperature time series	[0 , 90] days
D	factor of the assumed groundwater level	[$-\infty$, 0]
Δt_wshift	time shift of the assumed groundwater level time series	[-182 , 182] days
linear trend	corresponding linear increase due to linear decline groundwater table	[0 , ∞]
f_0	uncertainty of dv/v estimation	[10^{-10}, 10^{10}]

3.5 Selection of the optimal model

We evaluate the quality of models by the Akaike information criterion (AIC, Akaike, 1974) and the Bayesian information criterion (BIC, Schwarz, 1978). AIC and BIC are both metrics used for model selection, helping to choose the best model among a set of candidates by balancing model fit and complexity, which is penalized by the number of model parameters *k*. AIC evaluates models based on how well they fit the data, penalizing more complex models to avoid overfitting. Lower AIC values indicate a better model, suggesting a good fit with minimal complexity. Similar to AIC, BIC also penalizes model complexity but does so more strongly and significantly as the sample size increases. It is more conservative than AIC in selecting models, often favoring simpler models. Like AIC, lower BIC values suggest a better model. In addition to the two models mentioned in Section 3.4 (Equations 5, 6, 7), we also test them by keeping only SM-EWT or temperature in both models to see how they perform when we exclude either. The number of model parameters, *k*, in the linear-trend and lowpass models mentioned in Section 3.4 is 5 and 6, respectively. When we test them by keeping only the SM-EWT term, the *k* is 3 and 4. When we test them by keeping only the temperature term with a time shifting, the *k* is 4 and 5. In general, the combination of hydrological and thermoelastic terms gives a better fit.

The best fit of the testing models (Figures S8 and S9) is determined by the best likelihood model over a range of sampling. The AIC and BIC analyses (Figure 6) suggest that the lowpass model (magenta points) better explains the data for most stations. The subplots (d) and (e) in Figure 7 show the fitting results of the two models, respectively, at two example stations, MPU and SRU, with their input time series in subplots (a-c). At Station MPU, the long-term dv/v pattern is captured and well explained by the lowpass model.

However, at some stations, the AIC and BIC values for different models are very close to or even overlap with each other. This suggests that the performance of those models is at the same level. For instance, the results of the linear-trend and lowpass models at Station SRU closely match the dv/v data, making using the smooth groundwater level unnecessary. At some stations, models may just not explain the data, for instance, at stations HMU and NLU, as shown in Figures S10 and S11. Sometimes, this suggests the models perform as well as each other, for instance, seeing the blue and magenta points overlap at Station SRU in Figure 6. In the case of Stations MPU and CTU, the distinct distribution in AIC and BIC values demonstrates the success of the lowpass model. The factors of the optimal model are summarized in Figure S9 and Table S2.

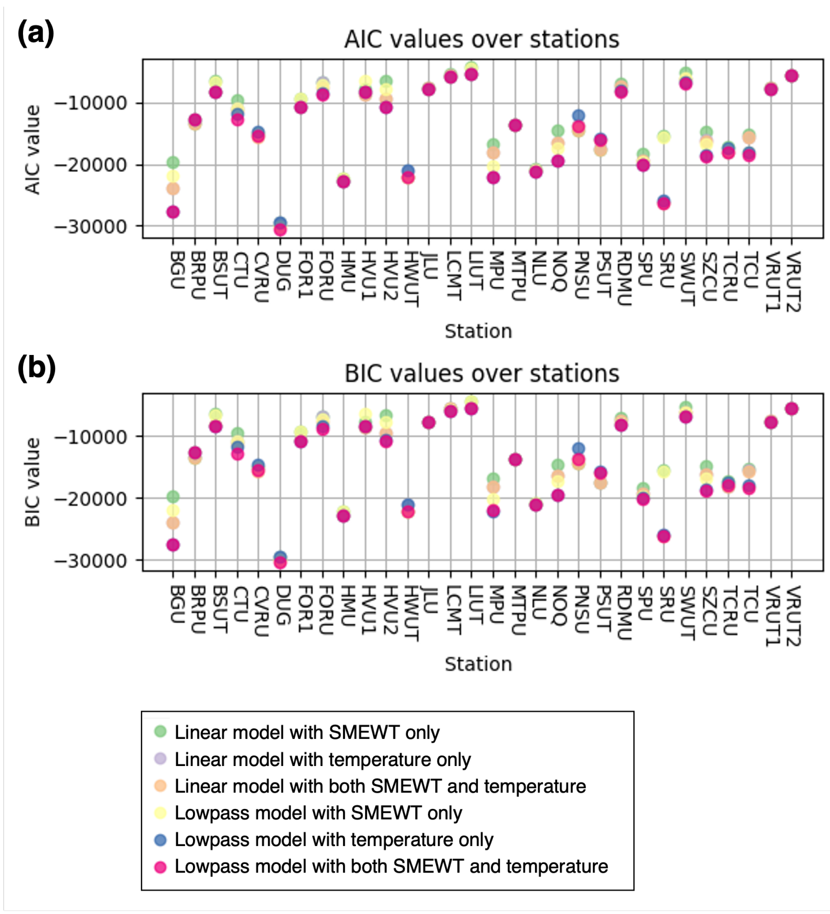

Figure 6. The (a) AIC and (b) BIC analyses across stations. The colors present the two models with different components involved.

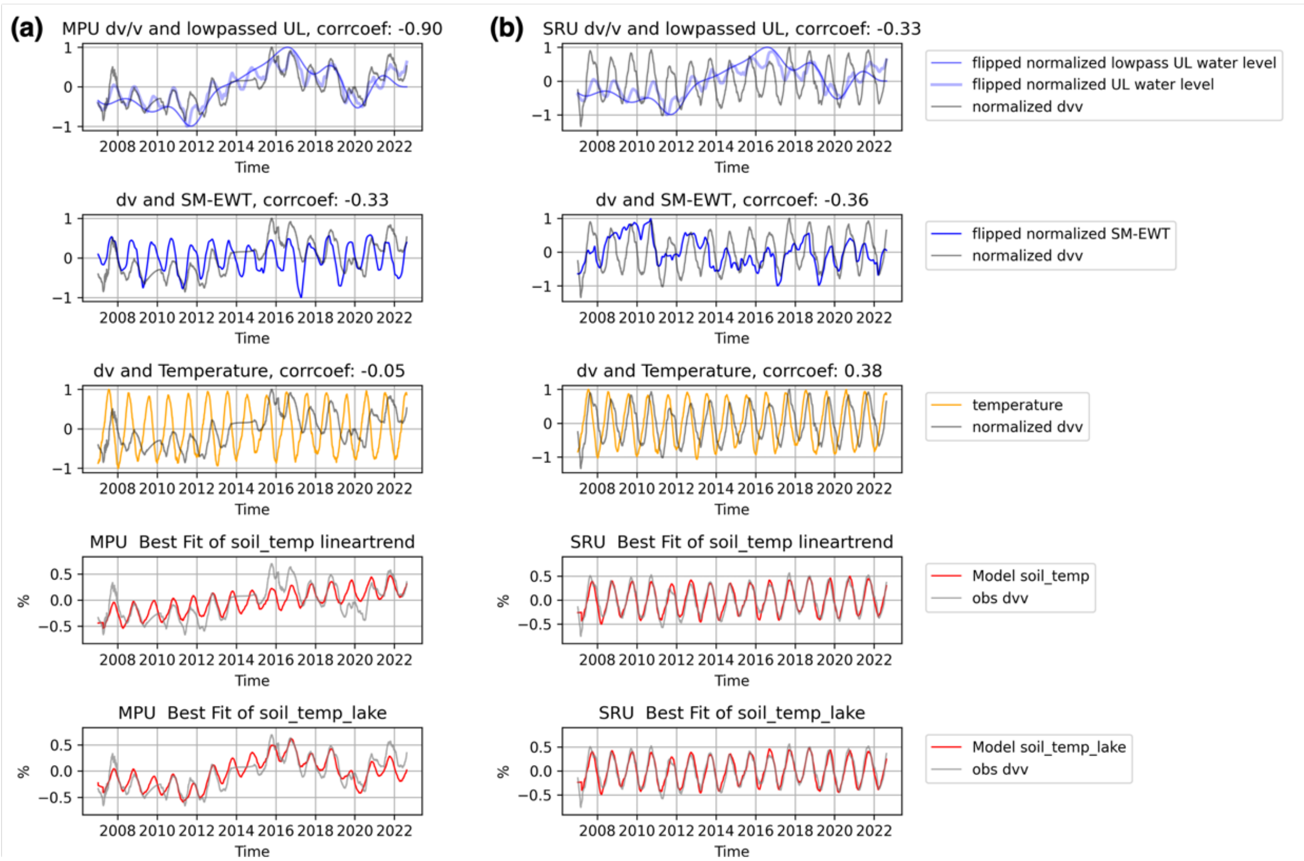

Figure 7. The modeling time series of Stations (a) MPU and (b) SRU. In both (a) and (b), the subplots from top to bottom are the normalized terms used in the model fitting process: the normalized dv/v (grey curves), flipped Utah Lake water level (thin blue curves), lowpass lake water level (thick blue curves), flipped SM-EWT (dark blue curves), temperature records (orange curves), and the optimal fit of the linear-trend and lowpass models (red curves).

4 Discussion

4.1 dv/v fluctuations and local site conditions

The dv/v behaviors across stations provide helpful information for understanding the general near-surface processes at different regions of the state. Figure S6 shows the amplitude of annual dv/v variations across stations. While the amplitude of each station is quite different, those stations in the GSL watershed show an increasing pattern from the northwest (i.e., BGU, SPU, HWUT) to the southeast (i.e., NOQ, TCU, MPU), except for stations near the Jordanelle Reservoir (JLU), Mill Creek (CTU), and on the north side of the lake (HVU). The dv/v observed at stations outside the GSL watershed seem to have no spatially coherent pattern. This may explain why the site dependency of dv/v at different locations will be affected by the most apparent feature if there is no primary impact factor controlling the system.

To further explore, the soil type information from the Utah Geospatial Resource Center (https://opendata.gis.utah.gov, last accessed 07/2024) and Vs30 values (Heath et al., 2020) at each station were collected and summarized in Table S3. Throughout the comparison (Figure S12), no clear relationship was found between dv/v amplitude and soil type, annual temperature, or SM-

EWT changes. However, a higher correlation (0.61) was observed with Vs30, indicating seismic characteristics may play a role.

4.2 (No) regional pattern

Utah has a semi-arid or desertic climate with micro-climates related to the diverse topography and surface water. The hydrological year typically starts October 1st, when precipitation returns after a dry summer. The regional pattern is that fall and winter have precipitation, especially heavy winter snow that slowly replenishes the surface and groundwater during snowmelt. Water storage recharges in spring and depletes over the summer due to high air temperatures and low precipitation summers. For most stations, the annual dv/v cyclicity (Figures 3c and S7) typically starts with a decrease at around late September and early October, which is consistent with the beginning of hydrological year cycles. This decrease in dv/v continues until next April and May when it reaches its lowest point of the year, which may indicate the highest groundwater level or near-surface water content in a year. After that, dv/v increases and goes into the following cycles. Snowmelt, as the primary source of stream and groundwater replenishment in the mid-west US, may align with the peak of dv/v stacks. Despite these qualitative arguments, we cannot draw a quantitative interpretation from the lack of spatial patterns. For instance, we do not observe a distinct relationship between times of lowest or highest dv/v and geographical consideration: correlation is weak between elevation, slope, and aspect given the location of the sensors and a 30s (~ 1 km) Digital Elevation Map, for which we chose SRTM15+V2.6 from Tozer et al. (2019). We only found a weak anticorrelation (-0.24) between the time of maximum dv/v (lowest groundwater levels) and the slope, which we interpret as an earlier depletion in the mountainous regions where snow melts in the spring and flows downward to the plains, and a later groundwater depletion in the plain area (i.e., a later replenishing and delayed depletion). Future investigations of groundwater pathways from the mountainous regions down to the plains could better inform our interpretation.

The co-evolution of observed dv/v and the water level between the GSL and Utah Lake reveals the resolvability of regional seismic stations on water resource monitoring at specific places, such as the GSL watershed. Although lacking comparable groundwater well data, we use lake levels as a proxy for the groundwater levels (Dogan et al., 2008; Evans et al., 2020; Javadzadeh et al., 2020). A higher correlation is observed for Utah Lake potentially because the GSL water level is more affected by anthropogenic activities and agriculture groundwater usage as water travels from the mountains, across population centers, and then enters the lake. Utah Lake is upstream of the GSL and connected through the Jordan River. As the terminal lake of the entire watershed, the GSL is more influenced by agricultural water and other economic activities and may not fully reflect the variation in regional subsurface water. Some stations' dv/v have higher correlation coefficients to the Utah Lake water level than the GSL.

It is worth noting that precipitation, snowmelt, soil moisture, groundwater table, and the lake's water level are all interconnected through a complex hydrological system. Even air temperature controls the evaporation from the surface water and moisture in the vadose zone (i.e., Chen et al., 2020; Benson and Dirmeyer, 2021). Our comparison indicates that most stations may observe the combination of groundwater signals and local subsurface moisture. The high correlation between dv/v and the three comparable hydrological data is revealed, but the unclear relationship among terms still needs further investigation.

4.3 What is the dominant effect on dv/v?

The values of the factors that best fit the lowpass model are shown in Figure S9 and summarized in Table S2. The coefficients are calculated to fit equation 7 and with normalized time series for each factor. Therefore, the coefficients capture a relative importance among the individual factors to predict dv/v. Coefficient *B*, related to the importance of subsurface soil moisture (Figure S9), shows a spatial pattern similar to the dv/v-moisture correlation (Figure 5c), as expected from the strong correlation. Stations with larger sensitivity to soil moisture tend to have lower Vs30 values, suggesting that lower velocities increase shallow depth sensitivities for dv/v, although this relationship is weak. The Vs30 model is a compiled model by the USGS. Given that the broadband stations used in this study are intentionally deployed on bedrock sites, with expected high Vs near the site, the reason for the weak correlation may be related to uncertainty in Vs30 or in the choice of Vs30 as a proxy for Vs structure in the entire site.

There is no particular spatial pattern in the best-fit values for *C*, the importance of thermoelastic effects, and Δt_{tshift}, the phase shift for thermoelastic stress that relates to thermal diffusion properties of the materials. This means we cannot draw a physical interpretation to predict common thermoelastic effects at these sites. These effects are attributed as unwanted when the goal is to address hydrological value; therefore, we do not further investigate this but treat it as a correction in the later analysis.

The pattern of coefficient *D*, the importance of the water table proxy (i.e., lake level), shows a spatial pattern in the GSL watershed, especially along the Wasatch Front. The time shift to the water table proxy reflects the phase difference between the local water table and the proxy water level. A group of stations had unsatisfactory results in fitting with the best-found shift at the boundary of our prior. Some of them have weak annual variations (e.g., VRUT). Some are strongly correlated with thermoelastic effects (e.g., SRU), subsurface moisture (e.g., CVRU), or other water bodies (e.g., JLU). Several stations are outside the GSL watershed and on higher elevations than the network average (e.g., BSUT, PNSU, MTPU). Ignoring these, we are left with 19 stations (circles in Figure 8) that exhibit a strong anti-correlation between the Δt_{wshift} and elevation (-0.64, Figure 8a). The trend can be explained by the gravity flow from the high-elevation snowmelt recharged water table down to the valley floor. The fact that we have positive Δt_{wshift} values may indicate that the lake experiences a faster recharge from rivers than from the groundwater. Thus, groundwater lags behind the lake seepage. We interpret that the groundwater table peaks around January to March at the high elevation and then in August to November in the valley floors. We thus interpret that the recharge is quite heterogeneous, with areas in the state that clearly lag behind surface water recharge. This implies a long-term gravity-driven flow that may be on the order of 19.2 m/month. Snowpack doesn't keep accumulating and melts all at once. It melts on some warm days, even in winter and spring. This may be a reason why the groundwater table peak at some stations is earlier than the general snowmelt season. Note that those high-elevation stations that fit the trend are still lower than those stations out of the trend (triangles in Figure 8), which are probably located above elevations where snowpack accumulated more over the winter.

The hydrological contribution to dv/v can be determined by correcting the mean level and thermoelastic effect from the observation. To explore the relative contributions between moisture and water table in explaining dv/v, we calculate the mixing ratios $R_{SMEWT} = -B/(|B| + |D|)$ and $R_{GW} = D/(|B| + |D|)$, respectively (Figure S13). The pattern of the mixing ratio shows that the groundwater contributes more at those stations in the GSL watershed. Others are varied in location. As a dynamic subsurface hydrological factor, the soil moisture content is a buffer as the groundwater recharge from the precipitation and hind runoff (Padilla et al., 2014; Dralle et al., 2018; Illien et al., 2021). Our approach of applying a low-pass filter to the lake level enables us to observe the rises and falls of the groundwater table on a relatively long-term scale. The residuals between the optimal model and observation can probably be explained by the shorter-time-scale groundwater level variations, which were lacking in this work. When complementary data becomes available, a more detailed investigation into near-surface water dynamics can be conducted. One other possible factor committed to the mixing ratios is the velocity structure below stations. Although the top 150-meter depth sensitivity is suggested in our measurements, the various velocity structures at stations may also dedicate the contribution to either moisture, which samples shallower perturbation more, or groundwater table, where relatively deeper perturbations are.

In general, these patterns demonstrate the site dependency and the uniqueness of the local dv/v. Every station has its major contributing terms to the modeling, and it is difficult to draw general behavior from this data, which is quite similar to previous studies (Viens et al., 2018; Clements and Denolle, 2023). Our modeling results suggest that although the groundwater table has generally declined over the past decades, using lake levels as proxies for the groundwater table successfully estimated groundwater flow time and length scales. However, using downstream lake levels as a proxy for local groundwater seems well justified and fits our seismic observation.

4.4 The observed dv/v and in situ groundwater variations

The dv/v time series and the observed groundwater level variation at a well near Station HVU show a strong correlation (0.69) in 2010-2022 (Figure S5). A slight shift (~1.4 months) between the two records may be owing to the distance (~12.3 km) between the seismic station and the groundwater well location. The high correlation coefficient and the similarity between the two time-series data suggest the ability to use passive seismic interferometry to study and monitor the near-surface hydrological properties (i.e., groundwater level variations) or even water dynamics in this specific region if a denser local seismic array is applicable.

At Station DUG, despite being closer (~6.8 km) to a well than Station HVU, the correlation coefficient between dv/v measurements and the groundwater data is only 0.39. Considering the expected lateral sensitivity of our dv/v measurements (~1 km), the distance between the station and the well is still too far. The local water usage/recharge may heavily influence a single-point measurement and might explain our observed discrepancy.

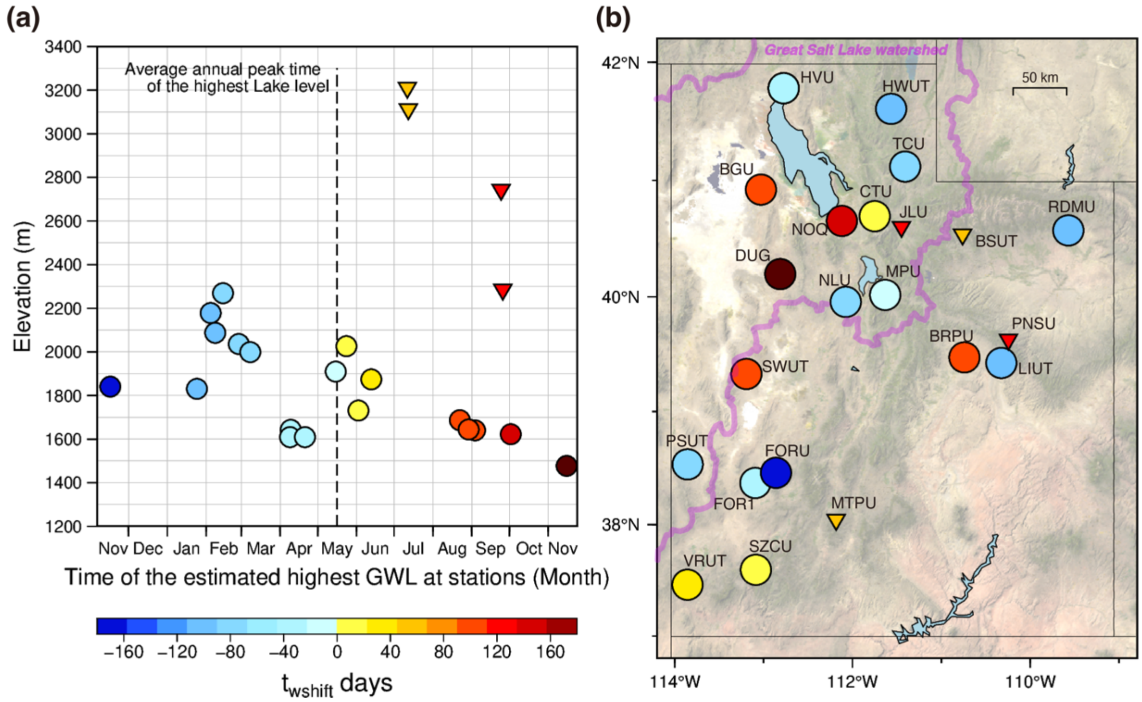

Figure 8. The distribution of the best-found Δt_{wshift} to the (a) station elevation and (b) station locations. The circles represent the stations with relatively low elevations (separate two clusters in (a)) compared to relatively high ones (triangles).

4.5 The dv/v response to large fluctuations of a nearby reservoir

Station JLU is severely affected by the Jordanelle Reservoir, showing a different behavior from other stations (Figure 2d). The two models we proposed in Section 2.5 do not fit the observation at Station JLU at all (Figure S8). It implies that the primary factor driving dv/v here is the other major hydrological component, the reservoir. Therefore, we test another model using the base model $y_{base}(t)$ and reservoir water level with time shifting allowed in a range of [-182, 182] days, finding a well-converged solution with a shift of 49.5 days. The fitting results (Figure S14) are improved, although the model is still unable to fit the data very well.

We note that the water level variation of the Jordanelle Reservoir (blue curves, Figure 2d) is considerable, about an order of magnitude larger than that of GSL and Utah Lake. Considering the relatively small surface area of the reservoir (~10 km^2), the dv/v variation of JLU hence might reflect the subsurface pore pressure response to a point water source (i.e., similar to a hydrological slug test but on a large scale).

5 Conclusions

We use time-lapse passive seismic interferometry to examine the near-surface hydrological processes through continuous seismic observation. We conduct a series of analyses on continuous seismic recordings from 28 broadband seismic stations across Utah State, covering the period between January 2006 and March 2023. We apply a single-station method to determine the temporal evolution of dv/v. Our dv/v findings uncovered distinct seasonality and long-term variations across stations. We explore these dv/v patterns by comparing the observed dv/v evolutions with two major surface water bodies in this area (i.e., the GSL and Utah Lake) and near-surface water (i.e., SM-EWT).

Throughout the analyses, the average annual dv/v variations and peak time align closely with the state's regional water cycles, offering valuable insights into near-surface seismic properties and hydrological processes. Amplitude in dv/v seasonality may be primarily related to local site conditions, as the Vs30 at stations. Multi-year wet-dry cycles are captured by those stations within the GSL watershed. The high correlation between dv/v and groundwater level, using lake levels as proxies, indicates that both are sensitive to the same controlling factor. Later, we explore the dv/v evolution using two linear models. We test two different groundwater level assumptions to account for the long-term declines in groundwater over the years. The modeling results suggest that a linear trend is too simple to estimate the pattern of the declining groundwater table. We take a lowpass filtering lake level as the assumption of long-term groundwater table variations in the model. In general, this model gives a better explanation of dv/v.

This study highlights the feasibility of monitoring and understanding hydrological processes in semi-arid regions using time-lapse passive seismic interferometry. With ongoing climate change, it is crucial to have effective management strategies to ensure the sustainable use of resources for society and the environment. A major limitation of this study, also pointed out in Clements and Denolle (2023), is the challenging lack of spatial correlation between dv/v given the sensor spacing. Further studies should build stronger hydrological models to establish if the spatial heterogeneity observed is explained by the spatial heterogeneity of the subsurface water and its dynamics over seasons.

Acknowledgments

This work was supported by the Ministry of Science and Technology of Taiwan (Grant 111-2917-I-564-008) and the National Science Foundation of the US under award number OAC-2103701 and grant EAR-1753362. Figures are produced using Generic Mapping Tools (GMT, Wessel et al., 2019) and Matplotlib (Hunter, 2007). We perform a Python tool *disab* (Luu, Computer software, https://doi.org/10.5281/zenodo.3987395) to obtain the depth sensitivity kernels.

Open Research

The seismic waveform data is from the IRIS data services (https://ds.iris.edu/ds/nodes/dmc/data/). The Great Salt Lake water level data is from the USGS Water Resources (https://waterdata.usgs.gov/nwis, Site No. 10010100). The two groundwater well records are from the USGS-Utah Water Science Center (https://www.usgs.gov/centers/utah-water-science-center, Site No. 414411112543701 and 401312112442301). The Utah Lake data is from the Snowpack Telemetry Network (SNOTEL, https://www.nrcs.usda.gov/resources/data-and-reports/snow-and-water-interactive-map, Utah reservoir site 10166500) maintained by the Natural Resources Conservation Service, U.S. Department of Agriculture (USDA). The soil moisture equivalent water thickness data is from the North American Land Data Assimilation System project phase 2 (NLDAS-2, https://doi.org/10.5067/WB224IA3PVOJ). The Jordanelle Reservoir water level data is from the United States Bureau of Reclamation (https://data.usbr.gov/time-series/search?v=1). The air temperature data is from the Parameter-elevation Relationships on the Independent Slopes Model (PRISM) Gridded Climate Data (https://prism.oregonstate.edu/). The soil characteristics are derived from the Utah Geospatial Resource Center (https://opendata.gis.utah.gov). Data of noise correlation functions and post-processing scripts are available on Harvard Dataverse (https://doi.org/10.7910/DVN/YCAAS4) and GitHub (https://github.com/kuanfufeng/Utah_Paper).

References

Akaike, H. (1974), A new look at the statistical model identification. *IEEE Transactions on Automatic Control*, *19(6)*, 716–723. https://doi.org/10.1109/TAC.1974.1100705

Baxter, B. K., & Butler, J. K. (2020). Climate change and great Salt Lake. *Great Salt Lake biology: a terminal lake in a time of change*, *23-52*. https://doi.org/10.1007/978-3-030-40352-2_2

Bennington, N., Haney, M., Thurber, C., & Zeng, X. (2018). Inferring magma dynamics at Veniaminof Volcano via application of ambient noise. *Geophysical Research Letters*, *45*(21), 11–650. https://doi.org/10.1029/2018GL079909

Benson, D. O., & Dirmeyer, P. A. (2021). Characterizing the relationship between temperature and soil moisture extremes and their role in the exacerbation of heat waves over the contiguous United States. *Journal of Climate*, *34*(6), 2175-2187. https://doi.org/10.1175/JCLI-D-20-0440.1

Berger, J. (1975), A note on thermoelastic strains and tilts, J. Geophys. Res., 80(2), 274–277. https://doi.org/10.1029/JB080i002p00274.

Chen, X., Li, Y., Chau, H. W., Zhao, H., Li, M., Lei, T., & Zou, Y. (2020). The spatiotemporal variations of soil water content and soil temperature and the influences of precipitation and air temperature at the daily, monthly, and annual timescales in China. *Theoretical and Applied Climatology*, *140*, 429-451. https://doi.org/10.1007/s00704-020-03092-9

Clements, T., & Denolle, M. A. (2018). Tracking groundwater levels using the ambient seismic field. *Geophysical Research Letters*, *45*(13), 6459-6465. https://doi.org/10.1029/2018GL077706

Clements, T., & Denolle, M. A. (2023). The Seismic Signature of California's Earthquakes, Droughts, and Floods. *Journal of Geophysical Research: Solid Earth*, *128*(1), e2022JB025553. https://doi.org/10.1029/2022JB025553

Colombi, A., Chaput, J., Brenguier, F., Hillers, G., Roux, P., & Campillo, M. (2014). On the temporal stability of the coda of ambient noise correlations. *Comptes Rendus Geoscience*, *346*(11-12), 307-316. https://doi.org/10.1016/j.crte.2014.10.002

Coumou, D., Rahmstorf, S. A decade of weather extremes. *Nature Clim Change 2*, 491–496 (2012). https://doi.org/10.1038/nclimate1452

Daly, C., Halbleib, M., Smith, J. I., Gibson, W. P., Doggett, M. K., Taylor, G. H., ... & Pasteris, P. P. (2008). Physiographically sensitive mapping of climatological temperature and precipitation across the conterminous United States. *International Journal of Climatology: a Journal of the Royal Meteorological Society*, *28*(15), 2031-2064. https://doi.org/10.1002/joc.1688

De Plaen, R. S., Lecocq, T., Caudron, C., Ferrazzini, V., & Francis, O. (2016). Single-station monitoring of volcanoes using seismic ambient noise. *Geophysical Research Letters*, *43*(16), 8511–8518.https://doi.org/10.1002/2016GL070078

Diewald, F., Denolle, M., Timothy, J. J., & Gehlen, C. (2024). Impact of temperature and relative humidity variations on coda waves in concrete. *Scientific Reports*, *14*(1), 18861. https://doi.org/10.1038/s41598-024-69564-4

Dogan, A., Demirpence, H., & Cobaner, M. (2008). Prediction of groundwater levels from lake levels and climate data using ANN approach. *Water Sa*, *34*(2), 199-208. https://hdl.handle.net/10520/EJC116518

Donaldson, C., Winder, T., Caudron, C., & White, R. S. (2019). Crustal seismic velocity responds to a magmatic intrusion and seasonal loading in Iceland's Northern Volcanic Zone. *Science Advances*, *5*(11), eaax6642. https://doi.org/10.1126/sciadv.aax6642

Dralle, D. N., Hahm, W. J., Rempe, D. M., Karst, N. J., Thompson, S. E., & Dietrich, W. E. (2018). Quantification of the seasonal hillslope water storage that does not drive streamflow. *Hydrological processes*, *32*(13), 1978-1992. https://doi.org/10.1002/hyp.11627

Ermert, L. A., Cabral-Cano, E., Chaussard, E., Solano-Rojas, D., Quintanar, L., Morales Padilla, D., ... & Denolle, M. A. (2023). Probing environmental and tectonic changes underneath Mexico City with the urban seismic field. *Solid Earth*, *14*(5), 529-549. https://doi.org/10.5194/se-14-529-2023

Evans, S. W., Jones, N. L., Williams, G. P., Ames, D. P., & Nelson, E. J. (2020). Groundwater Level Mapping Tool: An open source web application for assessing groundwater sustainability. *Environmental Modelling & Software*, *131*, 104782. https://doi.org/10.1016/j.envsoft.2020.104782

Fan, Y., Miguez-Macho, G., Weaver, C. P., Walko, R., & Robock, A. (2007). Incorporating water table dynamics in climate modeling: 1. Water table observations and equilibrium water table simulations. *Journal of Geophysical Research: Atmospheres*, *112*(D10). https://doi.org/10.1029/2006JD008111

Feng, K. F., Huang, H. H., Hsu, Y. J., & Wu, Y. M. (2021). Controls on Seasonal Variations of Crustal Seismic Velocity in Taiwan Using Single-Station Cross-Component Analysis of Ambient Noise Interferometry. *Journal of Geophysical Research: Solid Earth*, *126*(11), e2021JB022650. https://doi.org/10.1029/2021JB022650

Fokker, E., Ruigrok, E., & Trampert, J. (2024). On the temperature sensitivity of near-surface seismic wave speeds: application to the Groningen region, the Netherlands. *Geophysical Journal International*, *237*(2), 1129-1141. https://doi.org/10.1093/gji/ggae102

Fokker, E., Ruigrok, E., Hawkins, R., & Trampert, J. (2021). Physics-based relationship for pore pressure and vertical stress monitoring using seismic velocity variations. *Remote Sensing*, *13*(14), 2684. https://doi.org/10.1093/gji/ggz228

Ford, T. W., & Quiring, S. M. (2019). Comparison of contemporary in situ, model, and satellite remote sensing soil moisture with a focus on drought monitoring. *Water Resources Research*, *55*, 1565–1582. https://doi.org/10.1029/2018WR024039

Foreman-Mackey, D., Hogg, D. W., Lang, D., & Goodman, J. (2013). emcee: the MCMC hammer. *Publications of the Astronomical Society of the Pacific*, *125*(925), 306. https://doi.org/10.1086/670067

Gassenmeier, M., Sens-Schönfelder, C., Delatre, M., & Korn, M. (2014). Monitoring of environmental influences on seismic velocity at the geological storage site for CO2 in Ketzin (Germany) with ambient seismic noise. *Geophysical Journal International*, *200*(1), 524-533. https://doi.org/10.1093/gji/ggu413

Gaubert-Bastide, T., Garambois, S., Bordes, C., Voisin, C., Oxarango, L., Brito, D., & Roux, P. (2022). High-resolution monitoring of controlled water table variations from dense seismic-noise acquisitions. *Water Resources Research*, *58*(8), e2021WR030680. https://doi.org/10.1029/2021WR030680

Goodman, J., & Weare, J. (2010). Ensemble samplers with affine invariance. *Communications in applied mathematics and computational science*, *5*(1), 65-80. https://doi.org/10.2140/camcos.2010.5.65

Hassan, D., Burian, S. J., Johnson, R. C., Shin, S., & Barber, M. E. (2023). The Great Salt Lake Water Level is Becoming Less Resilient to Climate Change. *Water Resources Management*, *37*(6-7), 2697-2720. https://doi.org/10.1007/s11269-022-03376-x

Heath, D. C., Wald, D. J., Worden, C. B., Thompson, E. M., & Smoczyk, G. M. (2020). A global hybrid VS 30 map with a topographic slope–based default and regional map insets. *Earthquake Spectra*, *36*(3), 1570-1584. https://doi.org/10.1177/8755293020911137

Hobiger, M., Wegler, U., Shiomi, K., & Nakahara, H. (2014). Single-station cross-correlation analysis of ambient seismic noise: Application to stations in the surroundings of the 2008 Iwate-Miyagi Nairiku earthquake. *Geophysical Journal International*, *198*(1), 90–109. https://doi.org/10.1093/gji/ggu115

Hotovec-Ellis, A. J., Shiro, B. R., Shelly, D. R., Anderson, K. R., Haney, M. M., Thelen, W. A., ... & Johanson, I. A. (2022). Earthquake-Derived Seismic Velocity Changes During the 2018 Caldera Collapse of Kīlauea Volcano. *Journal of Geophysical Research: Solid Earth*, *127*(2), e2021JB023324. https://doi.org/10.1029/2021JB023324

Hulme, M. (2014). Attributing weather extremes to 'climate change' A review. *Progress in Physical Geography*, *38*(4), 499-511. https://doi.org/10.1177/0309133314538644

Illien, L., Andermann, C., Sens-Schönfelder, C., Cook, K. L., Baidya, K. P., Adhikari, L. B., & Hovius, N. (2021). Subsurface moisture regulates Himalayan groundwater storage and discharge. *AGU Advances*, *2*(2), e2021AV000398. https://doi.org/10.1029/2021AV000398

Javadzadeh, H., Ataie-Ashtiani, B., Hosseini, S. M., & Simmons, C. T. (2020). Interaction of lake-groundwater levels using cross-correlation analysis: A case study of Lake Urmia Basin, Iran. *Science of The Total Environment*, *729*, 138822. https://doi.org/10.1016/j.scitotenv.2020.138822

Khatri, K. B., & Strong, C. (2020). Climate change, water resources, and potential adaptation strategies in Utah. *Salt Lake City, UT: Division of Water Resources, Utah Department of Natural.*

Landerer, F. W., & Swenson, S. C. (2012). Accuracy of scaled GRACE terrestrial water storage estimates. *Water resources research*, *48*(4). https://doi.org/10.1029/2011WR011453

Lecocq, T., Longuevergne, L., Pedersen, H. A., Brenguier, F., & Stammler, K. (2017). Monitoring ground water storage at mesoscale using seismic noise: 30 years of continuous observation and thermo-elastic and hydrological modeling. *Scientific reports*, *7*(1), 1-16. https://doi.org/10.1038/s41598-017-14468-9

Lobkis, O. I., & Weaver, R. L. (2001). On the emergence of the Green's function in the correlations of a diffuse field. *The Journal of the Acoustical Society of America*, *110*(6), 3011-3017. https://doi.org/10.1121/1.1417528

Luu, K. disba: Numba-accelerated computation of surface wave dispersion [Computer software]. https://doi.org/10.5281/zenodo.3987395

Mao, S., Lecointre, A., van der Hilst, R. D., & Campillo, M. (2022). Space-time monitoring of groundwater fluctuations with passive seismic interferometry. *Nature communications*, *13*(1), 4643. https://doi.org/10.1038/s41467-022-32194-3

Mitchell, K. E., Lohmann, D., Houser, P. R., Wood, E. F., Schaake, J. C., Robock, A., ... & Bailey, A. A. (2004). The multi-institution North American Land Data Assimilation System (NLDAS): Utilizing multiple GCIP products and partners in a continental distributed hydrological modeling system. *Journal of Geophysical Research: Atmospheres*, *109*(D7). https://doi.org/10.1029/2003JD003823

NLDAS project (2022), NLDAS Noah Land Surface Model L4 Monthly 0.125 x 0.125-degree V2.0, Edited by David M. Mocko, NASA/GSFC/HSL, Greenbelt, Maryland, USA, Goddard Earth

Sciences Data and Information Services Center (GES DISC), Accessed: [April 2023], https://doi.org/10.5067/WB224IA3PVOJ

Null, S. E., & Wurtsbaugh, W. A. (2020). Water development, consumptive water uses, and Great Salt Lake. *Great Salt Lake biology: A terminal Lake in a time of change*, 1-21. https://doi.org/10.1007/978-3-030-40352-2_1

Oakley, D. O., Forsythe, B., Gu, X., Nyblade, A. A., & Brantley, S. L. (2021). Seismic ambient noise analyses reveal changing temperature and water signals to 10s of meters depth in the critical zone. *Journal of Geophysical Research: Earth Surface*, *126*(2), e2020JF005823. https://doi.org/10.1029/2020JF005823

Obermann, A., Planès, T., Larose, E., Sens-Schönfelder, C., & Campillo, M. (2013). Depth sensitivity of seismic coda waves to velocity perturbations in an elastic heterogeneous medium. *Geophysical Journal International*, *194*(1), 372-382.

Obermann, A., Planès, T., Hadziioannou, C., & Campillo, M. (2016). Lapse-time-dependent coda-wave depth sensitivity to local velocity perturbations in 3-D heterogeneous elastic media. *Geophysical Journal International*, *207*(1), 59-66.

Okubo, K., Delbridge, B. G., & Denolle, M. A. (2024). Monitoring velocity change over 20 years at Parkfield. *Journal of Geophysical Research: Solid Earth*, *129*(4), e2023JB028084. https://doi.org/10.1029/2023JB028084

Ostrovsky, L. A., & Johnson, P. A. (2001). Dynamic nonlinear elasticity in geomaterials. *La Rivista del Nuovo Cimento*, *24*(7), 1–46. https://doi.org/10.1007/BF03548898

Pacheco, C., & Snieder, R. (2005). Time-lapse travel time change of multiply scattered acoustic waves. *The Journal of the Acoustical Society of America*, *118*(3), 1300-1310. https://doi.org/10.1121/1.2000827

Padilla, C., Onda, Y., Iida, T., Takahashi, S., & Uchida, T. (2014). Characterization of the groundwater response to rainfall on a hillslope with fractured bedrock by creep deformation and its implication for the generation of deep-seated landslides on Mt. Wanitsuka, Kyushu Island. *Geomorphology*, 204, 444-458. https://doi.org/10.1016/j.geomorph.2013.08.024

Perrone, D., & Jasechko, S. (2017). Dry groundwater wells in the western United States. *Environmental Research Letters*, *12*(10), 104002. https://doi.org/10.1088/1748-9326/aa8ac0

Planès, T., Larose, E., Margerin, L., Rossetto, V., & Sens-Schoenfelder, C. (2014). Decorrelation and phase-shift of coda waves induced by local changes: multiple scattering approach and numerical validation. *Waves in Random and Complex Media*, *24*(2), 99-125. https://doi.org/10.1080/17455030.2014.880821

PRISM Climate Group, Oregon State University, https://prism.oregonstate.edu, data created 17 April 2023, accessed 17 April 2023.

Richter, T., Sens-Schönfelder, C., Kind, R., & Asch, G. (2014). Comprehensive observation and modeling of earthquake and temperature-related seismic velocity changes in northern Chile with passive image interferometry. *Journal of Geophysical Research: Solid Earth*, *119*(6), 4747-4765. https://doi.org/10.1002/2013JB010695

Schmandt, B., Lin, F. C., & Karlstrom, K. E. (2015). Distinct crustal isostasy trends east and west of the Rocky Mountain Front. *Geophysical Research Letters*, *42*(23), 10-290. https://doi.org/10.1002/2015GL066593

Schwabe, K., Albiac, J., Connor, J. D., Hassan, R. M., & González, L. M. (Eds.). (2013). Drought in arid and semi-arid regions: A multi-disciplinary and cross-country perspective. *Springer Science & Business Media*. https://doi.org/10.1007/978-94-007-6636-5

Schwarz, G. (1978). Estimating the dimension of a model. *Annals of Statistics*, *6*(2), 461–464. https://doi.org/10.1214/aos/1176344136

Seats, K. J., Lawrence, J. F., & Prieto, G. A. (2012). Improved ambient noise correlation functions using Welch′s method. *Geophysical Journal International*, *188*(2), 513–523. https://doi.org/10.1111/j.1365-246X.2011.05263.x

Sens-Schönfelder, C., & Eulenfeld, T. (2019). Probing the in situ elastic nonlinearity of rocks with earth tides and seismic noise. *Physical review letters*, *122*(13), 138501. https://doi.org/10.1103/PhysRevLett.122.138501

Sens-Schönfelder, C., & Wegler, U. (2006). Passive image interferometry and seasonal variations of seismic velocities at Merapi Volcano, Indonesia. *Geophysical research letters*, *33*(21). https://doi.org/10.1029/2006GL027797

Shen, Z., Yang, Y., Fu, X., Adams, K. H., Biondi, E., & Zhan, Z. (2024). Fiber-optic seismic sensing of vadose zone soil moisture dynamics. *Nature Communications*, *15*(1), 6432. https://doi.org/10.1038/s41467-024-50690-6

Snieder, R., Grêt, A., Douma, H., & Scales, J. (2002). Coda wave interferometry for estimating nonlinear behavior in seismic velocity. *Science*, *295*(5563), 2253-2255. https://doi.org/10.1126/science.1070015

Solazzi, S. G., Lissa, S., Rubino, J. G., & Holliger, K. (2021). Squirt flow in partially saturated cracks: a simple analytical model. *Geophysical Journal International*, *227*(1), 680-692. https://doi.org/10.1093/gji/ggab249

Somers, L. D., & McKenzie, J. M. (2020). A review of groundwater in high mountain environments. *Wiley Interdisciplinary Reviews: Water*, *7*(6), e1475. https://doi.org/10.1002/wat2.1475

Takano, T., Nishimura, T., Nakahara, H., Ueda, H., & Fujita, E. (2019). Sensitivity of seismic velocity changes to the tidal strain at different lapse times: Data analyses of a small seismic array at Izu-Oshima volcano. *Journal of Geophysical Research: Solid Earth*, *124*(3), 3011-3023. https://doi.org/10.1029/2018JB016235

Tangdamrongsub, N., Han, S. C., Yeo, I. Y., Dong, J., Steele-Dunne, S. C., Willgoose, G., & Walker, J. P. (2020). Multivariate data assimilation of GRACE, SMOS, SMAP measurements for improved regional soil moisture and groundwater storage estimates. *Advances in Water Resources*, 135, 103477. https://doi.org/10.1016/j.advwatres.2019.103477

Tozer, B., Sandwell, D. T., Smith, W. H., Olson, C., Beale, J. R., & Wessel, P. (2019). Global bathymetry and topography at 15 arc sec: SRTM15+. *Earth and Space Science*, *6*(10), 1847-1864. https://doi.org/10.1029/2019EA000658

Tsai, V. C. (2011). A model for seasonal changes in GPS positions and seismic wave speeds due to thermoelastic and hydrologic variations. *Journal of Geophysical Research: Solid Earth*, *116*(B4). https://doi.org/10.1029/2010JB008156

Viens, L., Denolle, M. A., Hirata, N., & Nakagawa, S. (2018). Complex near-surface rheology inferred from the response of greater Tokyo to strong ground motions. *Journal of Geophysical Research: Solid Earth*, *123*(7), 5710-5729. https://doi.org/10.1029/2018JB015697

Voisin, C., Garambois, S., Massey, C., & Brossier, R. (2016). Seismic noise monitoring of the water table in a deep-seated, slow-moving landslide. *Interpretation*, *4*(3), SJ67-SJ76. https://doi.org/10.1190/INT-2016-0010.1

Wada, Y., Van Beek, L. P., Van Kempen, C. M., Reckman, J. W., Vasak, S., & Bierkens, M. F. (2010). Global depletion of groundwater resources. *Geophysical research letters*, *37*(20). https://doi.org/10.1029/2010GL044571

Wang, S. Y., Gillies, R. R., & Reichler, T. (2012). Multidecadal drought cycles in the Great Basin recorded by the Great Salt Lake: Modulation from a transition-phase teleconnection. *Journal of Climate*, *25*(5), 1711-1721. https://doi.org/10.1175/2011JCLI4225.1

Weaver, R. L., & Lobkis, O. I. (2004). Diffuse fields in open systems and the emergence of the Green's function (L). *The Journal of the Acoustical Society of America*, *116*(5), 2731-2734. https://doi.org/10.1121/1.1810232

Weaver, R. L., Hadziioannou, C., Larose, E., & Campillo, M. (2011). On the precision of noise correlation interferometry. *Geophysical Journal International*, *185*(3), 1384-1392. https://doi.org/10.1111/j.1365-246X.2011.05015.x

Wu, C., Wu, X., Lu, C., Sun, Q., He, X., Yan, L., & Qin, T. (2022). Characteristics and driving factors of lake level variations by climatic factors and groundwater level. *Journal of Hydrology*, *608*, 127654. https://doi.org/10.1016/j.jhydrol.2022.127654

Xia, Y., Mitchell, K., Ek, M., Cosgrove, B., Sheffield, J., Luo, L., ... & Lohmann, D. (2012). Continental-scale water and energy flux analysis and validation for North American Land Data Assimilation System project phase 2 (NLDAS-2): 2. Validation of model-simulated streamflow. *Journal of Geophysical Research: Atmospheres*, *117*(D3). https://doi.org/10.1029/2011JD016051

Xia, Y., Mitchell, K., Ek, M., Sheffield, J., Cosgrove, B., Wood, E., ... & Mocko, D. (2012). Continental-scale water and energy flux analysis and validation for the North American Land Data Assimilation System project phase 2 (NLDAS-2): 1. Intercomparison and application of model products. *Journal of Geophysical Research: Atmospheres*, *117*(D3). https://doi.org/10.1029/2011JD016048

Yates, A. S., Savage, M. K., Jolly, A. D., Caudron, C., & Hamling, I. J. (2019). Volcanic, coseismic, and seasonal changes detected at White Island (Whakaari) volcano, New Zealand, using seismic ambient noise. *Geophysical Research Letters*, *46*(1), 99-108. https://doi.org/10.1029/2018GL080580

Journal of Geophysical Research: Solid Earth

Supporting Information for

A decadal survey of the near-surface seismic velocity response to hydrological variations in Utah, United States

Kuan-Fu Feng[1,2], Marine Denolle[1], Fan-Chi Lin[2], and Tonie van Dam[2]

1 Department of Earth and Space Sciences, University of Washington, United States

2 Department of Geology and Geophysics, University of Utah, United States

Contents of this file

Figures S1 to S14

Tables S1 to S3

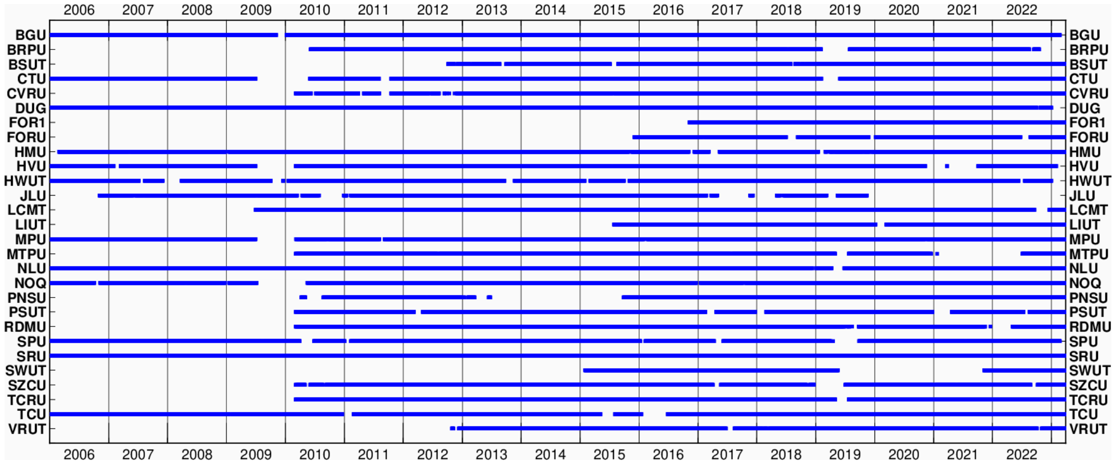

Figure S1. Data completeness of the 28 selected broadband seismic stations.

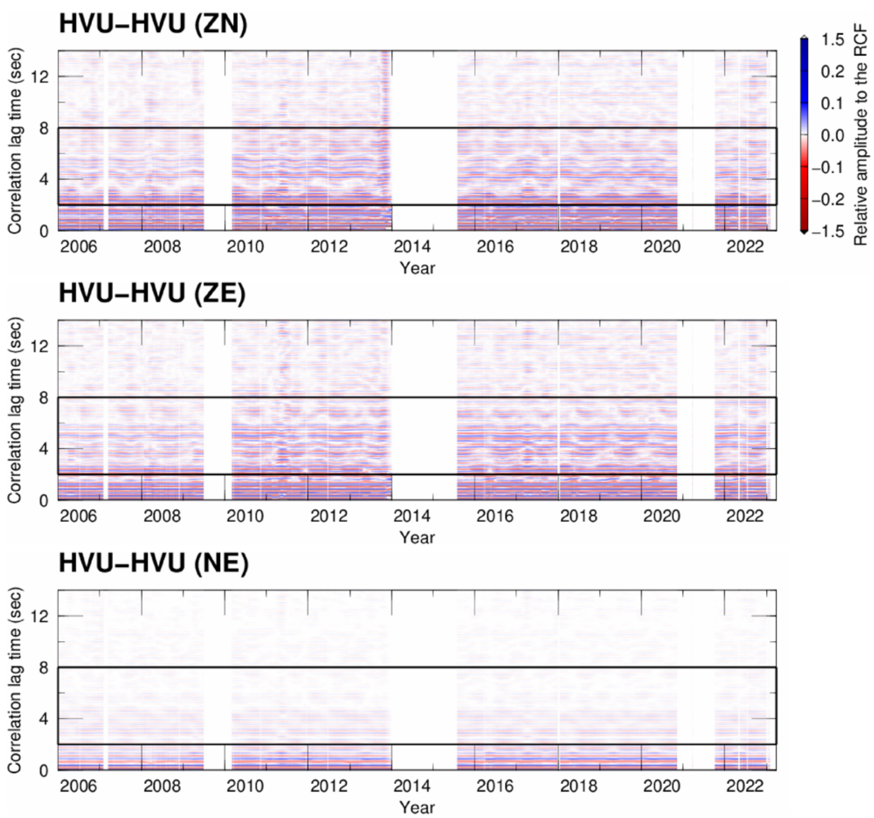

Figure S2. An example of single-station cross-component correlations (SC) at Station HVU. The black boxes denote the coda windows used for dv/v measuring. Different cross-component correlation functions are normalized by the peak amplitude of their corresponding reference functions, respectively.

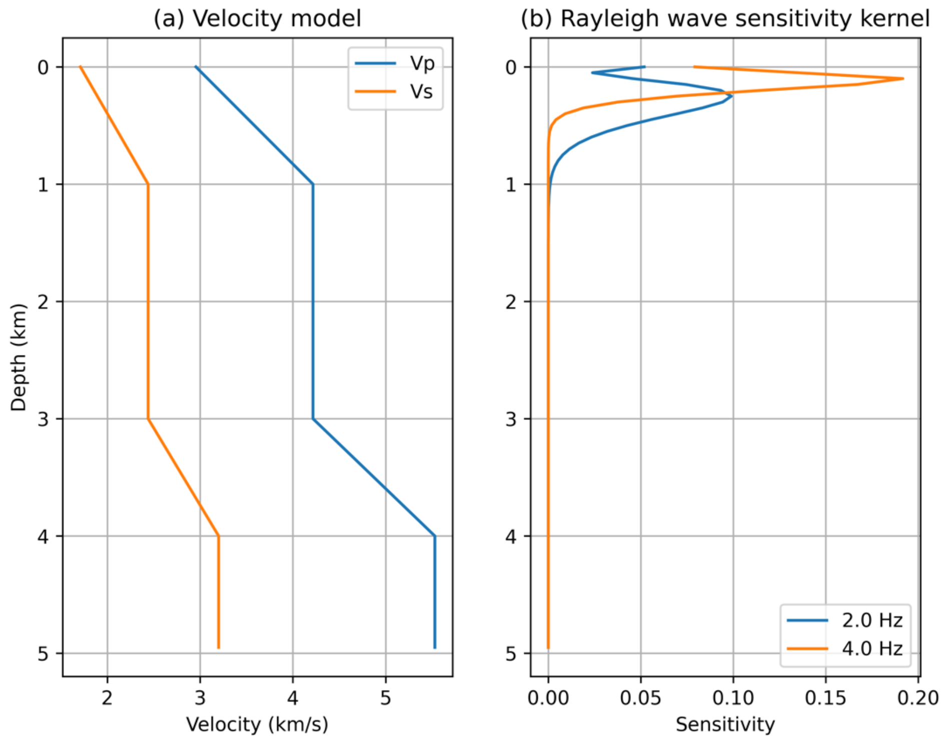

Figure S3. The reference velocity model and sensitivity kernels. The Vs. in (a) is the average value over the grids in proximity to stations from Schmandt et al. (2015). The Vp is assuming the Vp/Vs-ratio of 1.728. We perform a Python tool *disab* (Luu, Computer software, https://doi.org/10.5281/zenodo.3987395) to obtain the Rayleigh waves depth sensitivity kernels.

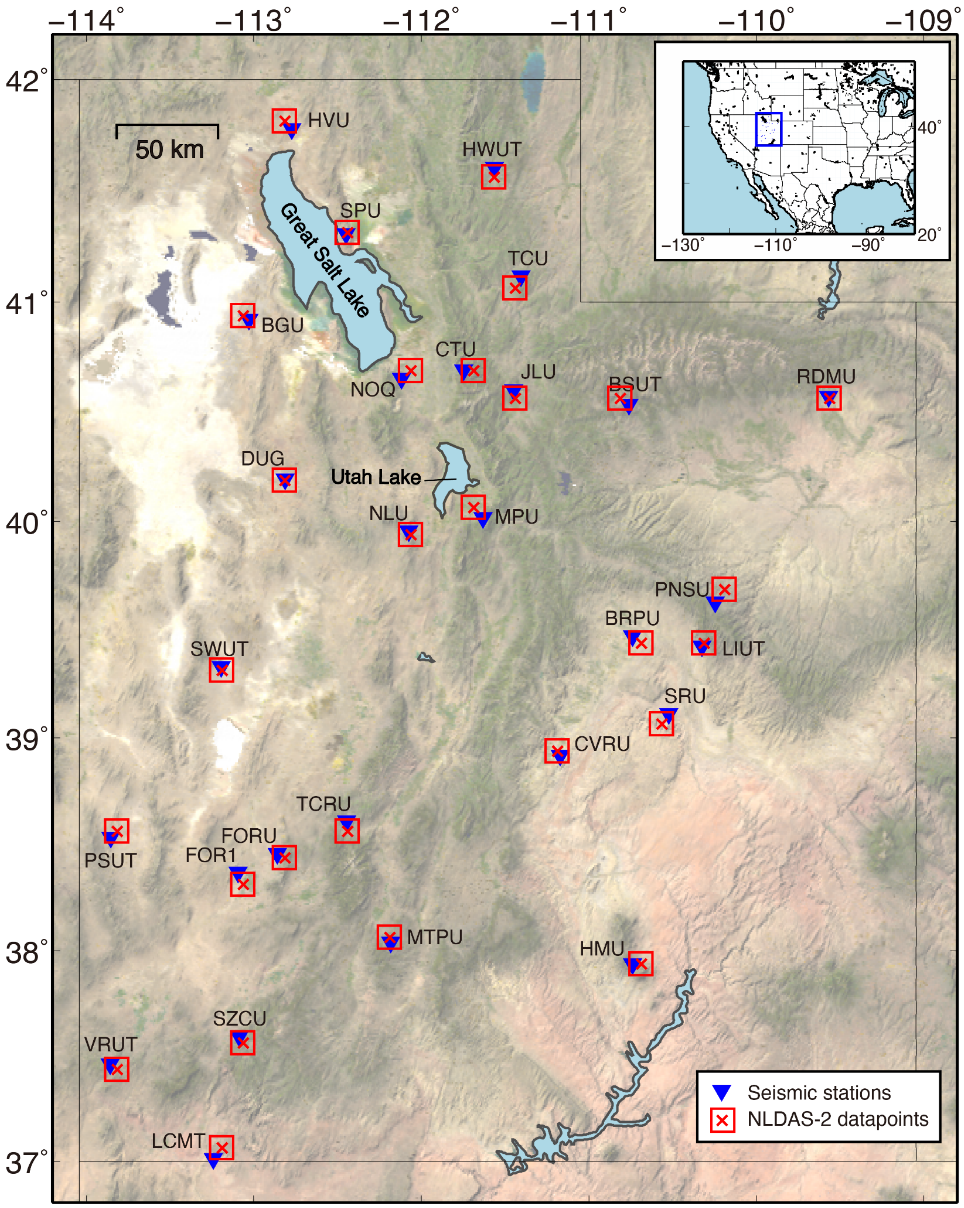

Figure S4. Seismic station location (inverted triangles) with the closest soil moisture equivalent water thickness (SM-EWT) data points (red square with a cross). The square circled the area of the selected grid data (0.125° x 0.125°) of the center of the cross.

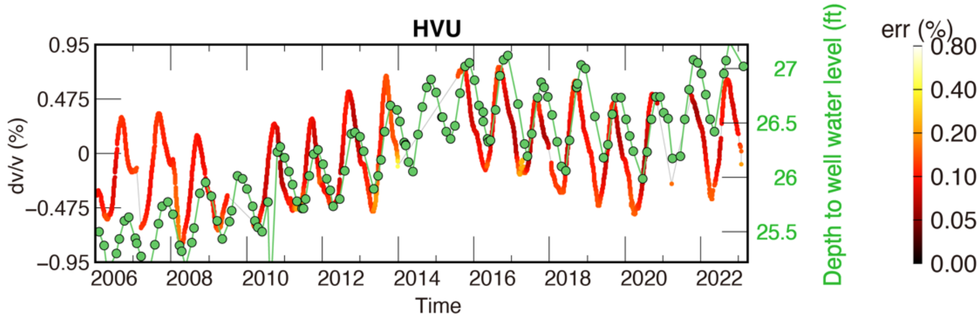

Figure S5. Time series of observed dv/v (red-color-coded curves) and the corresponding groundwater well level (green curves) at Station HVU.

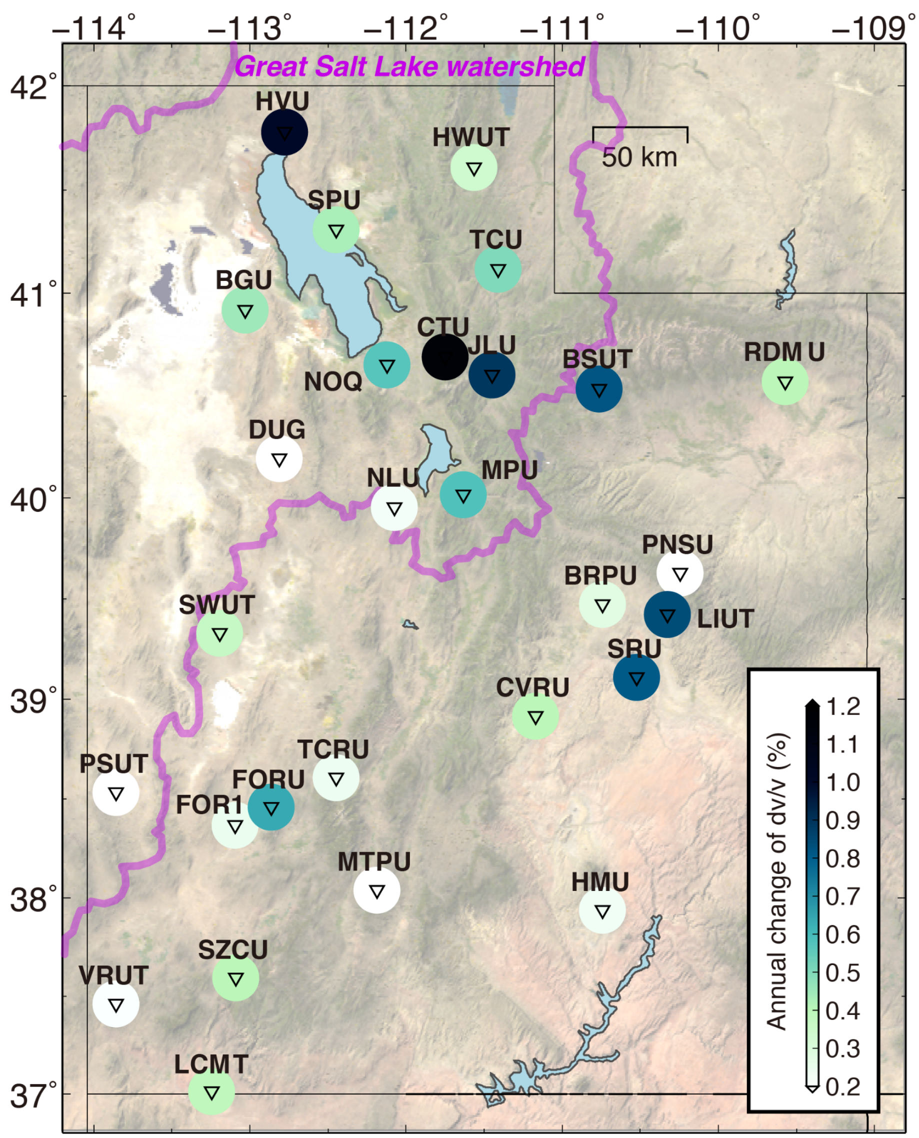

Figure S6. Amplitude map of the annual dv/v maximum variations.

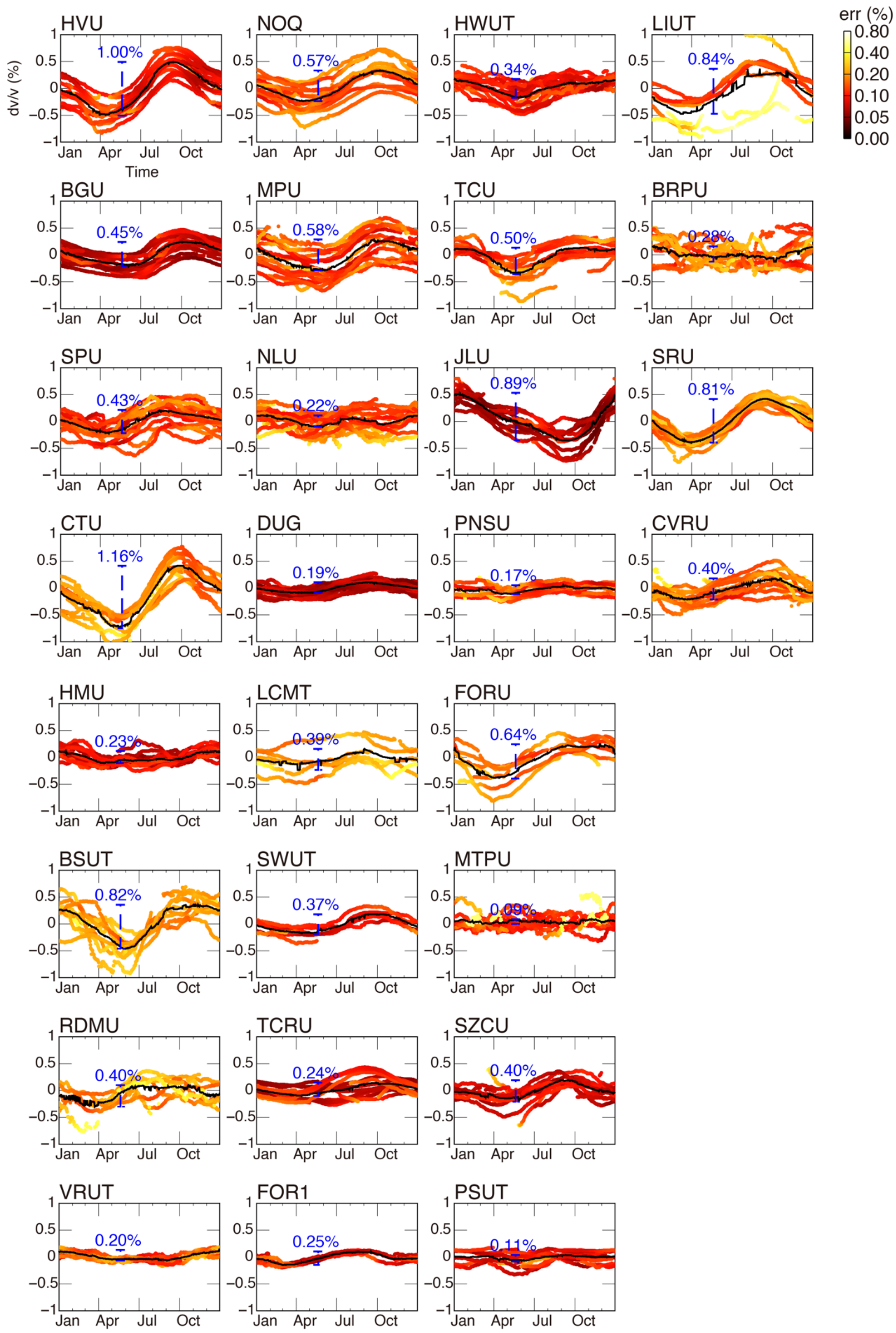

Figure S7. Annual time series plots of the dv/v across stations. The color-coded red curves are the observed dv/v represented at the annual scale. The black curves are the mean values of the annual variations. The annual amplitude is represented by the blue bars with the value marked on top.

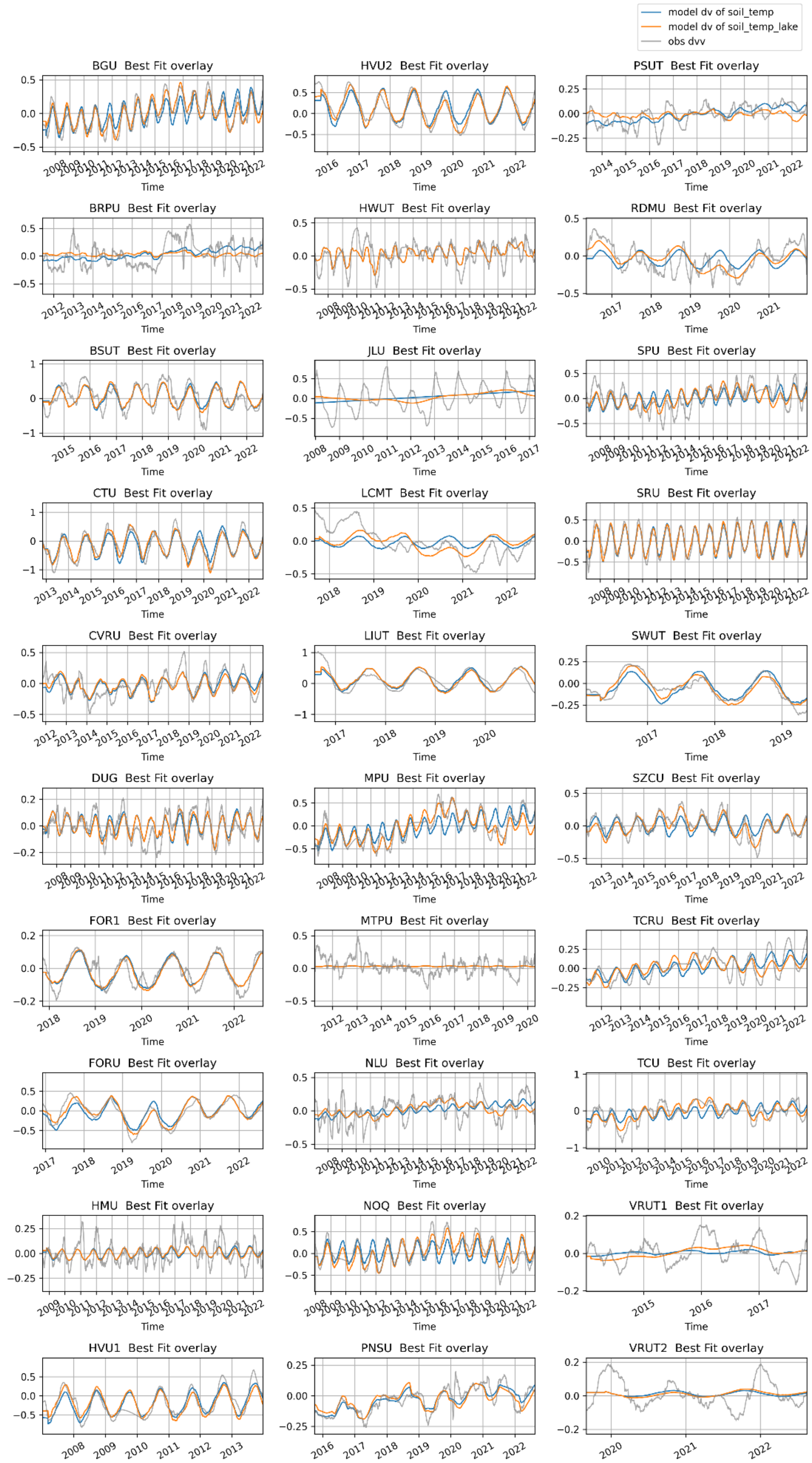
model dv of soil_temp
model dv of soil_temp_lake
obs dvv
BGU Best Fit overlay
HVU2 Best Fit overlay
PSUT Best Fit overlay
BRPU Best Fit overlay
HWUT Best Fit overlay
RDMU Best Fit overlay
BSUT Best Fit overlay
JLU Best Fit overlay
SPU Best Fit overlay
CTU Best Fit overlay
LCMT Best Fit overlay
SRU Best Fit overlay
CVRU Best Fit overlay
LIUT Best Fit overlay
SWUT Best Fit overlay
DUG Best Fit overlay
MPU Best Fit overlay
SZCU Best Fit overlay
FOR1 Best Fit overlay
MTPU Best Fit overlay
TCRU Best Fit overlay
FORU Best Fit overlay
NLU Best Fit overlay
TCU Best Fit overlay
HMU Best Fit overlay
NOQ Best Fit overlay
VRUT1 Best Fit overlay
HVU1 Best Fit overlay
PNSU Best Fit overlay
VRUT2 Best Fit overlay

Figure S8. The best fit of the two models. The gray curves are the observed dv/v. The blue and orange curves are the best fit of the linear-trend model and lowpass model, respectively.

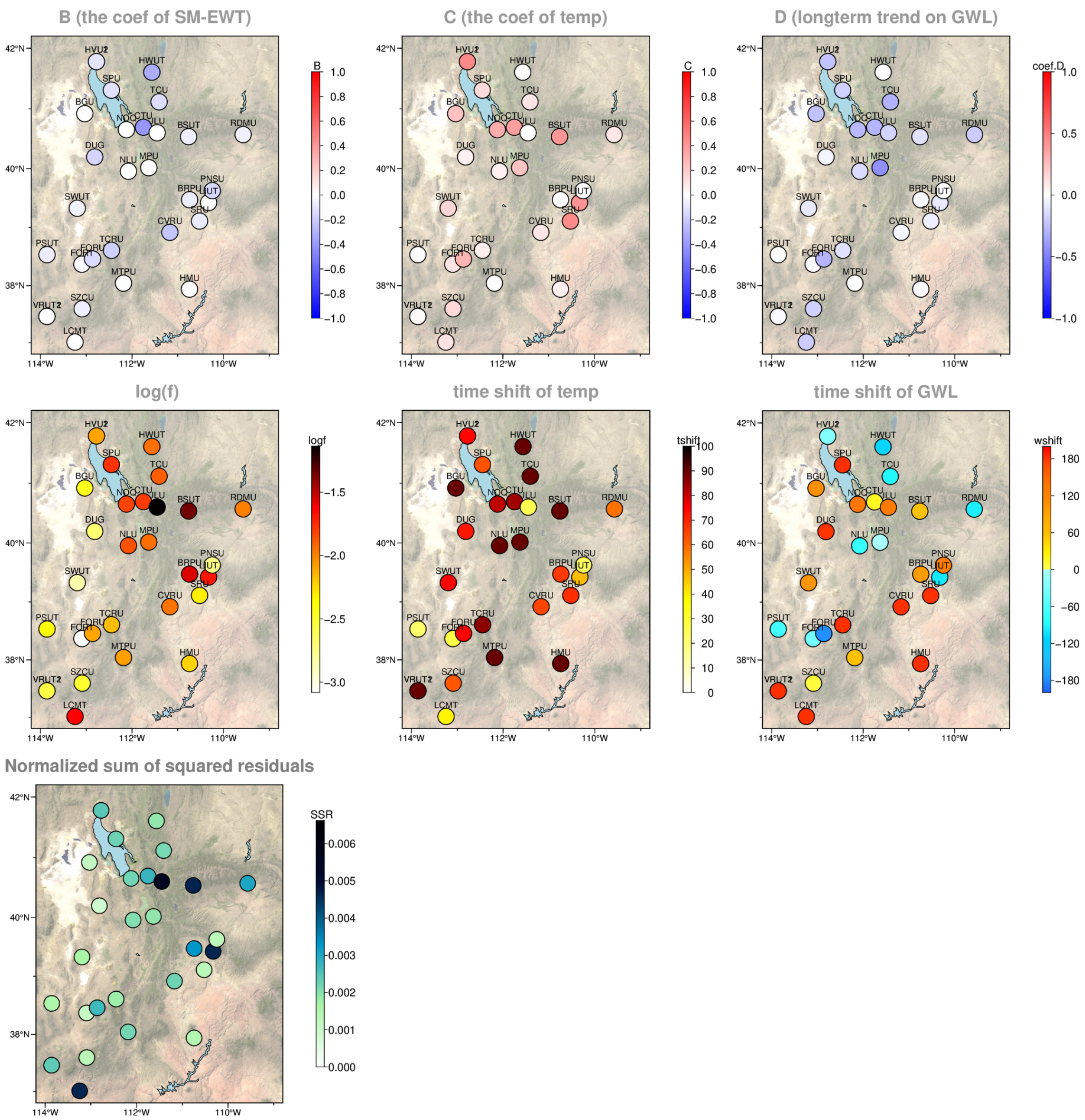

Figure S9. The factors that best fit the lowpass model are as follows: coefficient of SMEWT (*B*), Temperature (*C*), and GWL (*D*). The subplots in the middle row, from left to right, are the uncertainty of the dv/v estimation (*log(f)*), the time shift of the temperature term (*t_shift*), and the time shift of the GWL term (*w_shift*), respectively. Lastly, the normalized sum of the square residuals (*SSR*) at each station.

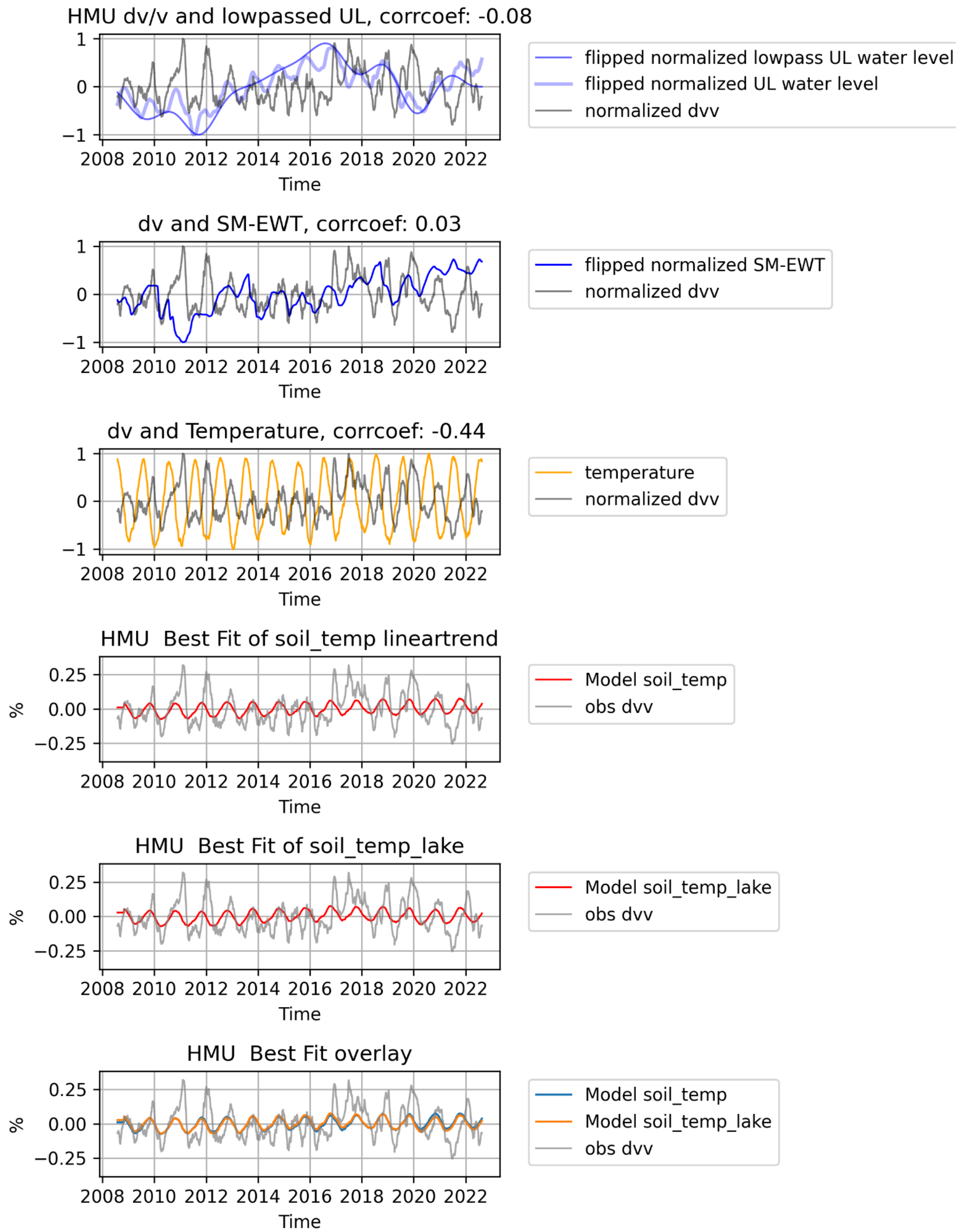

Figure S10. The time series of HMU station data and modeling results. The panels from top to bottom are the terms used in the fitting results of the linear-trend model (soil_temp) and lowpass model (soil_temp_lake).

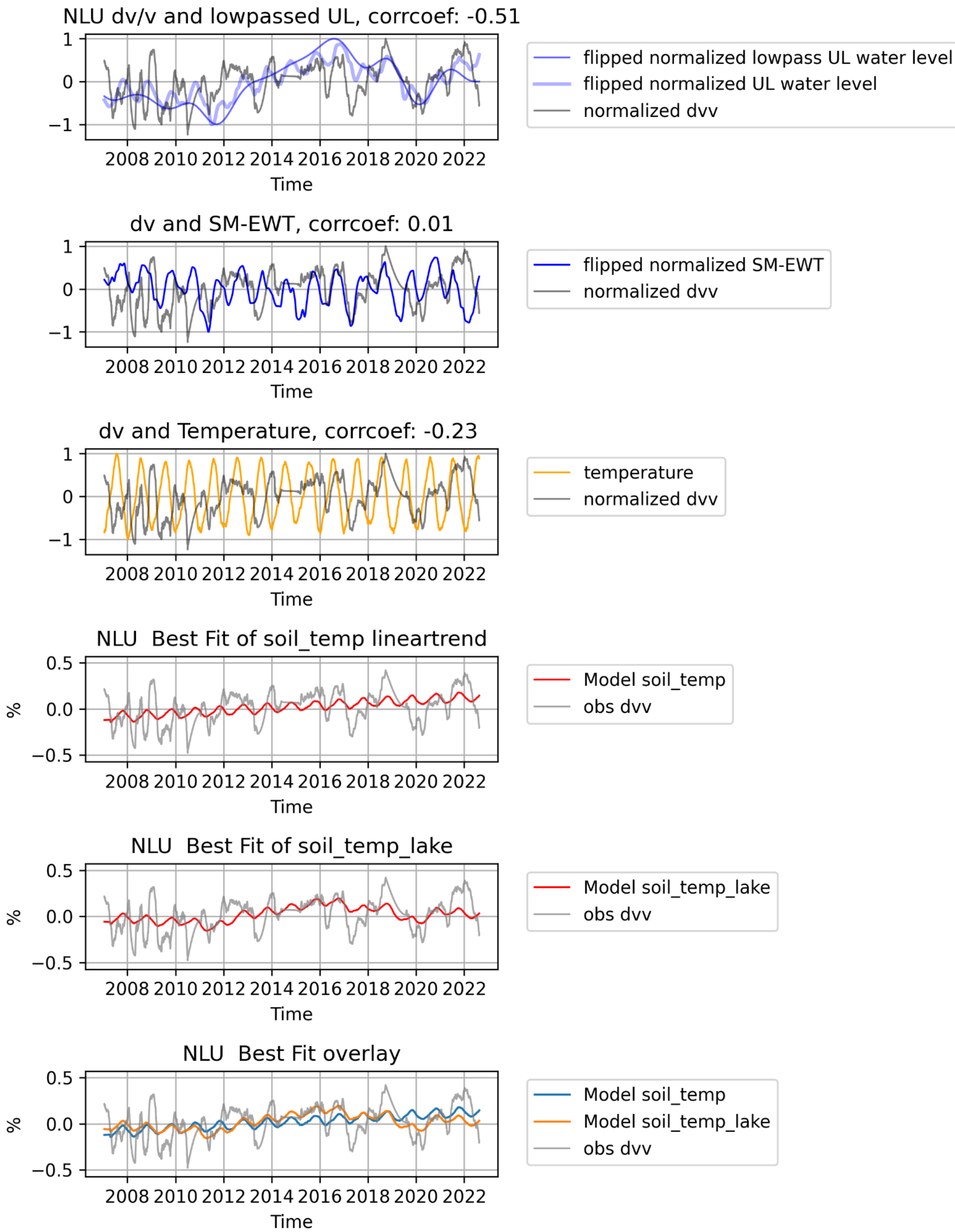

Figure S11. The time series of NLU station data and modeling results. The panels from top to bottom are the terms used in the fitting results of the linear-trend model (soil_temp) and lowpass model (soil_temp_lake).

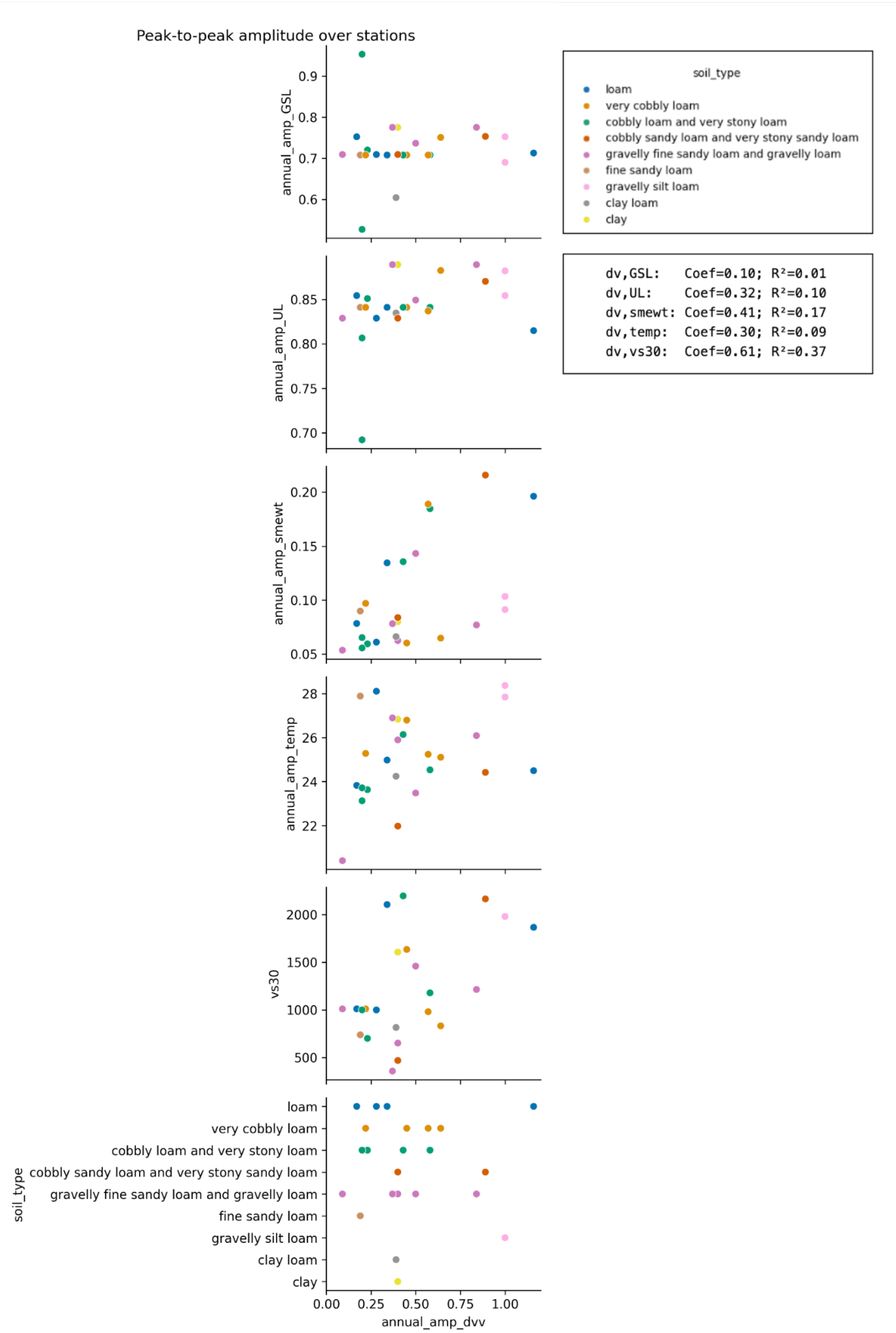
Peak-to-peak amplitude over stations
soil_type
loam
very cobbly loam
cobbly loam and very stony loam
cobbly sandy loam and very stony sandy loam
gravelly fine sandy loam and gravelly loam
fine sandy loam
gravelly silt loam
clay loam
clay
dv,GSL: Coef=0.10; R²=0.01
dv,UL: Coef=0.32; R²=0.10
dv,smewt: Coef=0.41; R²=0.17
dv,temp: Coef=0.30; R²=0.09
dv,vs30: Coef=0.61; R²=0.37
annual_amp_GSL
annual_amp_UL
annual_amp_smewt
annual_amp_temp
vs30
soil_type
annual_amp_dvv

Figure S12. Comparison of annual stacks' amplitude between dv/v and each factor, soil types, and Vs30 at station location. The color is corresponding to the soil type.

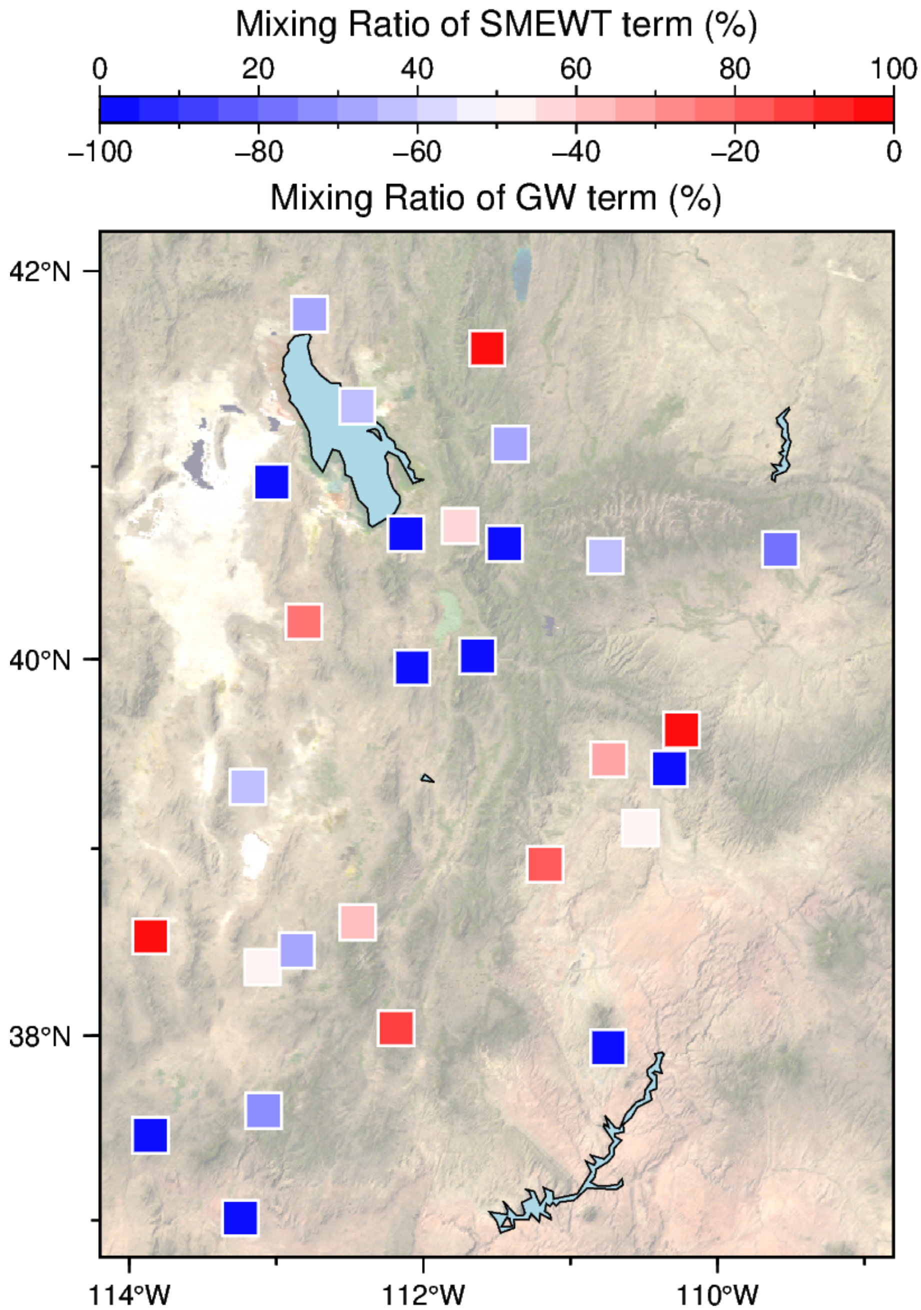

Figure S13. The mixing ratio map between the SM-EWT and GWL terms to explain the hydrological signal of dv/v. When the SM-EWT term dominates in fitted dv/v, the stations are color-coded with red. When the groundwater term dominates, the stations are color-coded in blue.

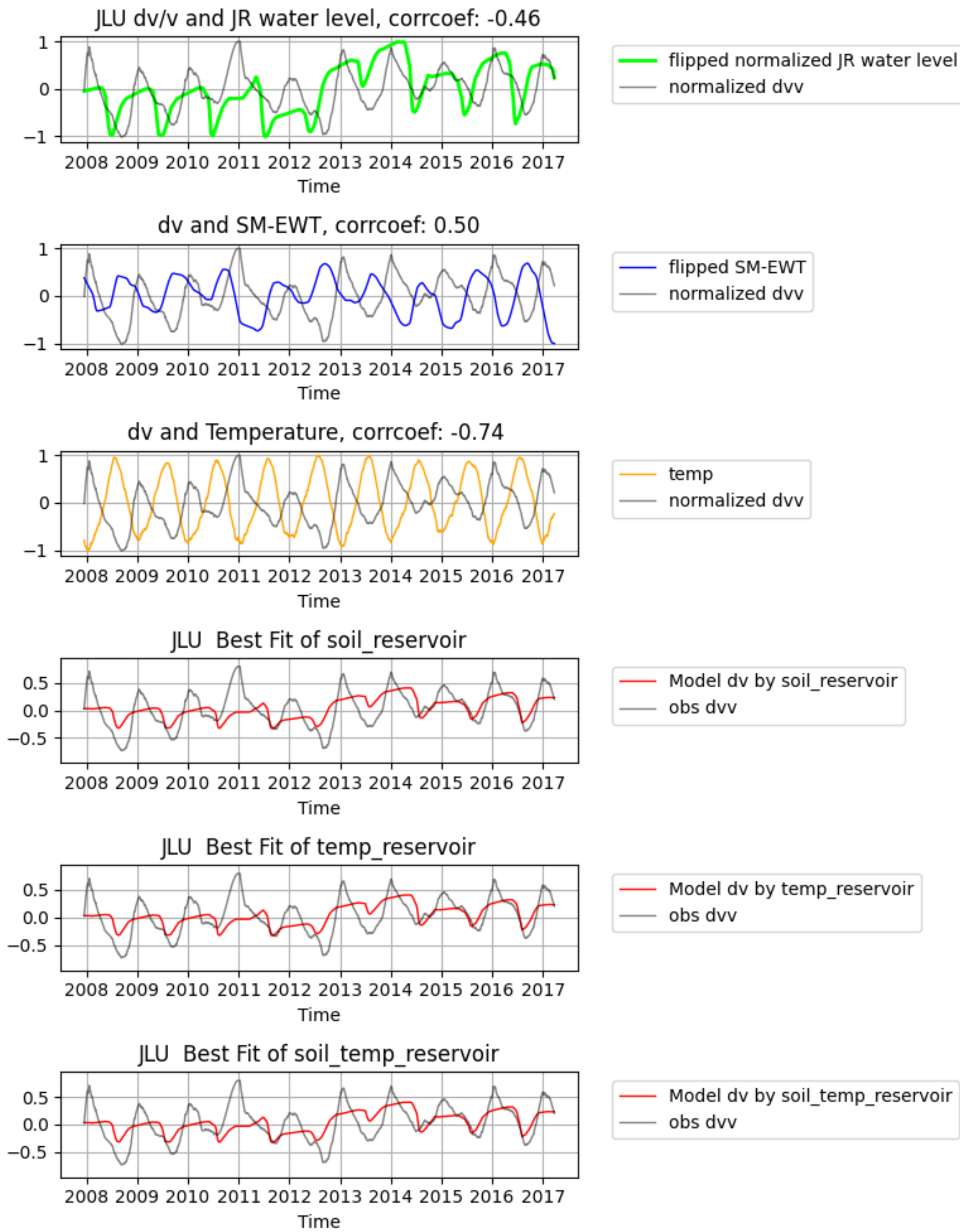

Figure S14. The time series of JLU station data and modeling results. The panels from top to bottom are the terms used in the fitting results of three testing scenarios. We replace the groundwater term in Equations 6 and 7 by the reservoir level (soil_temp_reservoir). We also test it by keeping only SM-EWT (soil_reservoir) or temperature (temp_reservoir) to see how they perform when we exclude either.

Table S1. The correlation coefficient and the R-squared values between the observed dv/v and the hydrological factors and temperature data. GSL: the Great Salt Lake water level. UTL: the Utah Lake water level. SM-EWT: soil moisture equivalent water thickness.

Station name	CC (dv,GSL)	R^2 (dv,GSL)	CC (dv,UTL)	R^2 (dv,UTL)	CC (dv,SM-EWT)	R^2 (dv,SM-EWT)	CC (dv,temp)	R^2 (dv,temp)
BGU	-0.67	0.45	-0.82	0.68	-0.24	0.06	-0.07	0.00
BRPU	-0.1	0.01	-0.06	0	-0.14	0.02	-0.21	0.04
BSUT	-0.24	0.06	-0.41	0.16	-0.15	0.02	-0.28	0.08
CTU	-0.59	0.34	-0.69	0.47	-0.78	0.6	0.04	0.00
CVRU	-0.03	0	0.04	0	-0.56	0.31	0.28	0.08
DUG	-0.23	0.05	-0.22	0.05	-0.62	0.38	0.29	0.08
FOR1	-0.17	0.03	-0.22	0.05	-0.6	0.36	0.72	0.52
FORU	-0.42	0.18	-0.43	0.19	-0.72	0.52	0.21	0.04
HMU	-0.03	0	-0.06	0	0.04	0	-0.44	0.19
HVU	-0.5	0.25	-0.65	0.43	-0.41	0.16	0.26	0.07
HWUT	-0.37	0.14	-0.34	0.12	-0.6	0.36	-0.28	0.08
JLU	-0.22	0.05	-0.24	0.06	0.53	0.28	-0.74	0.55
LCMT	0.35	0.12	-0.24	0.06	0.08	0.01	0.2	0.04
LIUT	0.13	0.02	-0.03	0	-0.34	0.11	0.28	0.08
MPU	-0.82	0.67	-0.91	0.82	-0.38	0.14	-0.05	0.00
MTPU	0.42	0.18	0.37	0.14	0.15	0.02	-0.1	0.01
NLU	-0.36	0.13	-0.48	0.23	-0.04	0	-0.23	0.05
NOQ	-0.4	0.16	-0.58	0.34	-0.42	0.17	0.09	0.01
PNSU	-0.01	0	0.32	0.11	-0.74	0.55	0.11	0.01
PSUT	-0.2	0.04	0.1	0.01	-0.29	0.08	-0.02	0.00
RDMU	-0.72	0.52	-0.58	0.34	-0.13	0.02	0.23	0.05
SPU	-0.47	0.22	-0.42	0.18	-0.44	0.19	0.23	0.05
SRU	-0.3	0.09	-0.34	0.12	-0.37	0.13	0.38	0.14
SWUT	-0.6	0.36	-0.68	0.46	-0.57	0.33	0.23	0.05
SZCU	-0.29	0.08	-0.58	0.34	-0.48	0.23	0.19	0.04
TCRU	-0.61	0.38	-0.53	0.28	-0.55	0.31	0.1	0.01
TCU	-0.53	0.28	-0.7	0.5	-0.52	0.27	-0.2	0.04
VRUT	-0.23	0.06	-0.13	0.02	0.08	0.01	-0.65	0.42

Table S2. The values of each factor in the optimal fit model. *A* is the mean level of dv/v. *B*, *C*, and *D* represent the coefficients of SMEWT, temperature, and lake level (estimated groundwater), respectively. Δt_{tshift} and Δt_{wshift} are the time shifts of the temperature and lake terms. *log(f)* is the uncertainty of the estimation. Normalized residuals are the residuals between the optimal model and the observation dv/v normalized by the data period of each station.

Station name	A	B (SMEWT)	C (temp)	Δt_{tshift}	D (GWL)	Δt_{wshift}	log(f)	normalized residuals
BGU	0.02	0.00	**0.24**	90.00	**-0.24**	108.57	-2.43	0.0012
BRPU	0.03	**-0.08**	0.00	66.68	-0.03	96.66	-1.56	0.0033
BSUT	0.05	-0.07	**0.41**	90.00	-0.11	55.25	-1.36	0.0047
CTU	-0.16	**-0.41**	0.38	84.32	-0.29	16.78	-1.79	0.0028
CVRU	-0.02	**-0.23**	0.10	64.71	-0.04	181.92	-1.95	0.0023
DUG	0.00	**-0.17**	0.05	71.60	-0.04	180.78	-2.67	0.0009
FOR1	-0.02	-0.02	**0.11**	27.19	-0.02	-36.58	-3.08	0.0011
FORU	0.01	-0.14	**0.29**	75.67	**-0.29**	-178.72	-2.10	0.0027
HMU	0.00	0.00	**0.06**	89.99	-0.02	181.90	-2.22	0.0015
HVU1	-0.19	0.00	**0.46**	63.36	-0.13	-37.07	-1.62	0.0039
HVU2	0.13	-0.10	**0.46**	74.43	-0.24	-25.42	-2.09	0.0024
HWUT	0.03	**-0.32**	0.01	90.00	0.00	-110.44	-1.94	0.0019
JLU	0.06	0.00	0.00	25.44	**-0.17**	130.49	-1.14	0.0055
LCMT	-0.01	0.00	0.11	38.99	**-0.20**	181.96	-1.61	0.0046
LIUT	0.12	0.00	**0.42**	47.42	-0.09	-99.69	-1.68	0.0046
MPU	-0.02	0.00	0.24	89.99	**-0.43**	-1.10	-1.94	0.0019
MTPU	0.03	0.00	0.01	89.91	0.00	56.12	-2.08	0.0022
NLU	0.02	0.00	0.06	89.99	**-0.14**	-77.56	-1.86	0.0021
NOQ	0.04	0.00	**0.33**	81.26	-0.27	136.79	-1.82	0.0022
PNSU	-0.03	**-0.15**	0.00	23.02	0.00	129.16	-2.74	0.0013
PSUT	-0.01	**-0.07**	0.00	22.08	0.00	-68.39	-2.36	0.0016
RDMU	-0.03	-0.06	0.09	58.39	**-0.21**	-96.06	-1.98	0.0030
SPU	0.02	-0.11	0.15	62.80	**-0.18**	181.98	-1.77	0.0023
SRU	0.01	-0.08	**0.46**	68.40	-0.07	181.81	-2.31	0.0013
SWUT	-0.06	-0.05	**0.17**	75.19	-0.09	103.62	-2.84	0.0017
SZCU	0.01	-0.06	0.15	62.22	**-0.18**	7.32	-2.50	0.0013
TCRU	0.02	**-0.19**	0.07	86.29	-0.12	181.99	-2.16	0.0018
TCU	-0.03	-0.13	0.11	90.00	**-0.30**	-89.92	-1.89	0.0022
VRUT1	0.00	0.00	0.01	89.99	**-0.03**	26.83	-2.78	0.0017

VRUT2	0.02	0.00	0.02	89.96	**-0.02**	182.00	-2.54	0.0024

Table S3. The annual amplitude values of dv/v, GSL water level, Utah Lake water level, SM-EWT, temperature, and the soil type, and Vs30 at Stations. The annual amplitudes are calculated over the corresponding periods to the seismic data. The soil types are from the Utah Geospatial Resource Center (https://opendata.gis.utah.gov). Its soil characteristics of Utah are derived from the SSURGO database. The Vs30 is from a global hybrid Vs30 map (Heath et al., 2020).

Station name	Annual amplitude of dv/v	Annual amplitude of GSL water level	Annual amplitude of UTL water level	Annual amplitude of SM-EWT	Annual amplitude of temperature	Soil type	Vs30 (m/s)
BGU	0.45	0.71	0.84	0.06	26.80	Very cobbly loam	1634.5
BRPU	0.28	0.71	0.83	0.06	28.11	Loam	999.5
BSUT	0.82	0.74	0.82	0.05	22.59	No data	2121.2
CTU	1.16	0.71	0.82	0.20	24.50	Loam	1866.9
CVRU	0.40	0.71	0.83	0.06	25.90	Gravelly fine sandy loam	650.5
DUG	0.19	0.71	0.84	0.09	27.89	Fine sandy loam	738.1
FOR1	0.25	0.60	0.83	0.08	25.79	No data	267.9
FORU	0.64	0.75	0.88	0.06	25.11	Very cobbly loam	831.7
HMU	0.23	0.72	0.85	0.06	23.63	Cobbly loam	700.5
HVU	1.00	0.75	0.85	0.10	28.37	Gravelly silt loam	1981.6
HWUT	0.34	0.71	0.84	0.13	24.98	Loam	2106.4
JLU	0.89	0.75	0.87	0.22	24.42	Cobbly sandy loam	2165.5
LCMT	0.39	0.60	0.83	0.07	24.25	Clay loam	814.9
LIUT	0.84	0.78	0.89	0.08	26.09	Gravelly loam	1213.8
MPU	0.58	0.71	0.84	0.18	24.54	Very stony loam	1178.2
MTPU	0.09	0.71	0.83	0.05	20.40	Gravelly fine sandy loam	1010.0
NLU	0.22	0.71	0.84	0.10	25.28	Very cobbly loam	1010.0
NOQ	0.57	0.71	0.84	0.19	25.24	Very cobbly loam	980.4
PNSU	0.17	0.75	0.85	0.08	23.83	Loam	1010.0
PSUT	0.11	0.72	0.81	0.07	24.41	No data	1001.9
RDMU	0.40	0.78	0.89	0.08	26.84	Clay	1606.6
SPU	0.43	0.71	0.84	0.14	26.14	Cobbly loam	2197.0
SRU	0.81	0.71	0.84	0.05	27.22	No data	1460.0
SWUT	0.37	0.78	0.89	0.08	26.90	Gravelly loam	356.8
SZCU	0.40	0.71	0.83	0.08	21.98	Very stony sandy loam	468.3
TCRU	0.24	0.71	0.83	0.10	23.69	No data	1010.0
TCU	0.50	0.74	0.85	0.14	23.48	Gravelly loam	1460.0
VRUT	0.20	0.95	0.81	0.06	23.13	Very stony loam	1000.0